Continuity in the Plastic Strain Rate and its Influence on Texture Evolution

Justin C. Mach[a], Armand J. Beaudoin[a,*], Amit Acharya[b]

[a]*Department of Mechanical Science and Engineering, University of Illinois at Urbana-Champaign, 1206 W. Green St., Urbana, IL 61801, USA*
[b]*Department of Civil and Environmental Engineering, Carnegie Mellon University, Pittsburgh, PA 15213, USA*

Abstract

Classical plasticity models evolve state variables in a spatially independent manner through (local) ordinary differential equations, such as in the update of the rotation field in crystal plasticity. A continuity condition is derived for the lattice rotation field from a conservation law for Burgers vector content—a consequence of an averaged field theory of dislocation mechanics. This results in a nonlocal evolution equation for the lattice rotation field. The continuity condition provides a theoretical basis for assumptions of co-rotation models of crystal plasticity. The simulation of lattice rotations and texture evolution provides evidence for the importance of continuity in modeling of classical plasticity. The possibility of predicting continuous fields of lattice rotations with sharp gradients representing non-singular dislocation distributions within rigid viscoplasticity is discussed and computationally demonstrated.

Key words: continuity, finite strain, viscoplastic material, crystal plasticity, dislocations

1. Introduction

It is well known that Taylor-type material point simulations of texture evolution tend to overestimate intensity and under-represent certain texture components at large deformations. The work of Hirsch and Lücke (1988) provides a comprehensive investigation of this for f.c.c. metals. Maximum intensities tend to be two or more times larger for simulation than experiment. The β fiber, which develops in f.c.c. metals undergoing plane strain compression is of particular interest as the prediction of components along this fiber, such as the brass and S components, tend to be weak with respect to the copper and Taylor components. Classical models of texture evolution warrant tremendous merit for their ability to capture general trends in large deformation processes of many metals. However, the subtle inconsistencies mentioned above indicate a fundamental problem in the simulation of orientation evolution and perhaps, as we will show, evolution of plastic flow as a whole.

It will be shown that a certain level of continuity required of the constitutively specified plastic velocity gradient can be interpreted as a continuity condition for the lattice rotation field in a rigid viscoplastic setting. This continuity condition implies a continuous lattice spin field (often referred to as the spin field hereafter) and has been dubbed co-rotation or co-spin. Techniques of this nature have been used in self-consistent material point simulations (Bolmaro

*Corresponding author. Tel. +1-217-244-9094; fax +1-217-244-6534
Email addresses: abeaudoi@illinois.edu (Armand J. Beaudoin)

et al., 2000; Tomé et al., 2002), also coupled with finite elements (Bolmaro et al., 2006; Signorelli et al., 2006) resulting in textures that are closer to experimental values. This also proved to be useful in predicting recrystallization textures by allowing for grain fragmentation through the co-rotation of neighboring segments of grains (Bolmaro et al., 2005). A commonality among these works is that the co-rotation methods tend to reduce the intensity of simulated textures and therefore match more closely with experimental results. The co-rotation methods require some or all of the components of the lattice spin of neighboring grains (or parts of grains) to be equal. We will show that this continuity in the spin field is a limiting case of the continuity required of the plastic velocity gradient. We hope to show that models that utilize co-rotation, which are developed from experimental evidence or derived from compatibility or equilibrium equations, are sensible and physically reasonable models.

We will derive a condition of continuity for the spin field, in a finite deformation setting, obtained from a continuity condition associated with a mesocale PDE model of plasticity, referred to as Mesoscale Field Dislocation Mechanics (MFDM). MFDM is a result of averaging the evolution equation of excess dislocation (ED) density from the microscopic theory of continuous distribution of dislocations (Acharya and Roy, 2006). The ED density (also referred to as the Nye tensor) is an averaged measure of geometrically necessary dislocations (GNDs), which is in contrast to the statistically stored dislocation (SSD) density which carries no net sign. The ED and SSD densities both contribute to plastic flow, however the ED density may also contribute to long-range stress effects (Roy and Acharya, 2006; Varadhan, 2007). MFDM provides a precise link between this microscopic theory and classical elastic-plastic modeling of permanent deformation. In doing so, it views the evolution of the Nye tensor as a balance law for Burgers vector content, which implies a partial continuity condition on the plastic rate of deformation at material surfaces of discontinuity; as is well known, conventional plasticity theory poses no restrictions on a surface of discontinuity beyond displacement and traction continuity for quasistatic deformations (these conditions also being included in the new framework). Here, material surfaces have only the requirement that their normal velocity field coincide with the normal component of the velocity of the material particles with which the surface coincides instantaneously. Thus, they could be grain boundaries, but are not required to be so. The new condition has also arisen in the work of Gurtin and Needleman (2005), but not as a consequence of a fundamental balance law, and with a major difference in interpretation in that they assume that the partial continuity is to be automatically expected in solutions of the conventional theory, whereas we do not. It is noteworthy that Mathur and Dawson (1989) used a continuous description of the rotation field which was not motivated by continuity but rather because the rotation was integrated along streamlines in an Eulerian formulation. To ensure that the rotation remained orthogonal they used a two-point integration method with a local interpolation of the Euler angles over finite elements.

It is the intention of the present effort to make a statement pertinent *to the plasticity problem in general* following from a well-founded conservation statement drawn from the continuum theory of distributed dislocations. That is, this work is not to be viewed as an alternative modeling approach adopting gradients in some fashion, but rather as an expression of the boundary value problem. The specific choice of texture evolution in a rigid-viscoplastic material is selected as a specific vehicle for illustrating the implications of the continuity condition through evolution of material

state.

An example will help to compare what is implied by conventional plasticity and MFDM. We begin with the fundamental equation of incompatibility, $\boldsymbol{\alpha} = -\mathrm{curl}\left(\boldsymbol{F}^{e-1}\right)$, where $\boldsymbol{\alpha}$ is the excess dislocation density. Let a grain boundary be oriented perpendicular to the direction $\boldsymbol{e_N}$ with $(\boldsymbol{e_R}, \boldsymbol{e_T}, \boldsymbol{e_N})$ forming a right-handed triad, as shown in Fig. 1. Then, performing standard pill box arguments (cf. Appendix A and Acharya (2007), Sec. 4) for pill-surfaces

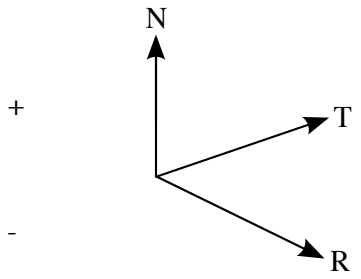

Figure 1: Grain boundary dividing grains '+' and '-'.

oriented perpendicular to the R and T directions and localizing to the grain boundary, we have

$$\begin{aligned} \boldsymbol{F}^{e-1}_{+}\,\boldsymbol{e}_R - \boldsymbol{F}^{e-1}_{-}\,\boldsymbol{e}_R = \boldsymbol{\alpha}\,\boldsymbol{e}_T \quad &\Rightarrow \quad [\![\, \boldsymbol{F}^{e-1} \,]\!]\,\boldsymbol{e}_R = \boldsymbol{\alpha}\,\boldsymbol{e}_T \\ -\boldsymbol{F}^{e-1}_{+}\,\boldsymbol{e}_T + \boldsymbol{F}^{e-1}_{-}\,\boldsymbol{e}_T = \boldsymbol{\alpha}\,\boldsymbol{e}_R \quad &\Rightarrow \quad [\![\, \boldsymbol{F}^{e-1} \,]\!]\,\boldsymbol{e}_T = -\boldsymbol{\alpha}\,\boldsymbol{e}_R \end{aligned} \tag{1}$$

if the dislocation density field is singularly supported on the grain boundary and

$$\begin{aligned} [\![\, \boldsymbol{F}^{e-1} \,]\!]\,\boldsymbol{e}_R = \boldsymbol{0} \\ [\![\, \boldsymbol{F}^{e-1} \,]\!]\,\boldsymbol{e}_T = \boldsymbol{0} \end{aligned} \tag{2}$$

if the dislocation density field is even in the least bit spread out in the direction perpendicular to the grain boundary. We can write

$$[\![\, \boldsymbol{F}^{e-1} \,]\!] = [\![\, \boldsymbol{F}^{e-1} \,]\!]\,\boldsymbol{e}_R \otimes \boldsymbol{e}_R \;+\; [\![\, \boldsymbol{F}^{e-1} \,]\!]\,\boldsymbol{e}_T \otimes \boldsymbol{e}_T \;+\; [\![\, \boldsymbol{F}^{e-1} \,]\!]\,\boldsymbol{e}_N \otimes \boldsymbol{e}_N\,, \tag{3}$$

so that,

$$[\![\, \boldsymbol{F}^{e-1} \,]\!] \times \boldsymbol{e}_N = -\,[\![\, \boldsymbol{F}^{e-1} \,]\!]\,\boldsymbol{e}_R \otimes \boldsymbol{e}_T \;+\; [\![\, \boldsymbol{F}^{e-1} \,]\!]\,\boldsymbol{e}_T \otimes \boldsymbol{e}_R \;=\; -\boldsymbol{\alpha}\,\boldsymbol{e}_T \otimes \boldsymbol{e}_T \;-\; \boldsymbol{\alpha}\,\boldsymbol{e}_R \otimes \boldsymbol{e}_R \tag{4}$$

in the case when the dislocation density field is singular on the grain boundary.

Thus by allowing arbitrary jumps in $\boldsymbol{F}^{e-1}$, conventional plasticity theory implies the existence of a singular surface distribution of dislocations. On the other hand, if we stipulate that even at scales of resolution appropriate to

macroscopic plasticity, singular distributions of dislocations are not allowed, i.e. grain boundary dislocations have some width perpendicular to the grain boundary, then the partial continuity

$$\left[\!\left[\boldsymbol{F}^{e-1} \right]\!\right] \times \boldsymbol{e}_N = \boldsymbol{0} \tag{5}$$

is implied. Both choices are plausible. Clearly, at scales of resolution appropriate for macroscopic crystal plasticity, admitting a singular distribution at a surface seems eminently reasonable (and, of course, is the standard model in classical dislocation theory with further localization to a curve in the surface). Mathematically, conventional crystal plasticity does not deal with any field equations for dislocation density and so such singular distributions are not a problem. Even in a static continuum theory of dislocations (i.e. elastic theory of continuously distributed dislocations) this is not a severe mathematical problem. However, in a dynamical theory of continuously distributed dislocations this can be a problem, as the balance law for Burgers vector content leads to a time-dependent PDE for the Nye tensor involving nonlinear functions of the Nye tensor and products. In this case most nonlinear combinations of singular distributions do not make mathematical sense. Thus, a plasticity theory that considers Nye tensor evolution as fundamental would lean towards accepting the partial continuity condition based on mathematical grounds. As we show in this paper, it turns out that this continuity leads to texture evolution results that are in better accord with physical observations.

We note here that the continuity condition (Eq. 5) does not preclude the development of a smooth, localized, but non-singular, dislocation distribution in our rigid-viscoplastic model, which for all practical purposes may be considered as defects localized on surfaces. As a slight digression, we also note the contrast of this situation with the elastic theory of phase transitions, where the elastic distortion is a genuine deformation gradient and in the case when this field is required to be a field of proper rotations, no inhomogeneity (and, in particular, a smoothed jump type) is allowed as a consequence of bulk deformation compatibility (e.g. Shield (1973)). Therefore, in this setting defects are allowed only through singular distributions at interfaces associated with a discontinuity in the deformation/displacement field and the deformation gradient does not satisfy a continuity condition of the type in Eq. 5. Clearly, the admissibility of an inhomogeneous, smooth, point-wise strain-free elastic distortion field in our model is a direct consequence of the fact that the (inverse) elastic distortion in a theory with continuously distributed dislocations is not required to be compatible in the bulk but, in the absence of singular dislocation density fields, is required to be compatible at interfaces[1].

The outline of the paper is as follows. In Section 2 we discuss the evolution of the excess density and the fact that it indicates tangential continuity of the constitutively specified plastic velocity gradient. Section 3 shows the implication of the continuity constraint in conventional elastic-plastic modeling, specifically in the setting of rigid crystal viscoplasticity. In this case, continuity in the lattice spin is indicated and from this we obtain a length-scale free nonlocal evolution equation for the lattice rotation field which has a notable influence on texture evolution. The

[1]AA thanks Kaushik Dayal for discussions on interfacial compatibility

connection between the continuity constraint derived herein and the co-rotation and relaxed constraint type models of crystal plasticity is established. In Section 4 we discuss the implementation of the continuity constraint in a 3D hybrid finite element code which utilizes a rate-dependent crystal viscoplastic constitutive model. Three applications for the analysis of the effect of the continuity constraint on texture evolution were simulated:

- Rolling of a polycrystal: The rolling textures from the nonlocal model reveal a weaker overall texture and more uniform β fiber compared with the local and Taylor model simulations—a result supported by experimental observation.
- Lattice rotation of individual grains: These simulations indicate that the lattice rotation in (at least) parts of a grain in a bulk sample may be strongly influenced by continuity required at the boundary, and provide evidence of grain splitting.
- Rolling of the S array: Plane strain compression of S-type grains in a periodic arrangement reveals a band of N-direction rotated cube orientations in the nonlocal result, associated with defect structures which form in the vicinity of the grain boundary.

The results and discussion regarding the simulations are presented in Section 5 and conclusions are given in Section 6.

2. Background

Field dislocation mechanics (FDM) (Mura, 1963; Acharya, 2004) suggests the following evolution equation for the excess dislocation density tensor, $\boldsymbol{\alpha}$, also known as Nye's tensor (Nye, 1953) (also referred to hereafter as the dislocation density tensor).

$$\dot{\boldsymbol{\alpha}} = -\mathrm{curl}\,(\boldsymbol{\alpha} \times \boldsymbol{V}) \tag{6}$$

The evolution equation is a conservation law for Burgers vector content (Acharya, 2001), where $\boldsymbol{V}$ is the velocity of the excess dislocation density. MFDM is an averaged model of FDM in which a connection between the theory of continuously distributed dislocations and classical elastoplasticity is established. We begin our discussion with the small deformation theory. The importance here lies in the following evolution equation for the dislocation density (Acharya and Roy, 2006),

$$\dot{\boldsymbol{\alpha}} = -\mathrm{curl}\,(\boldsymbol{\alpha} \times \boldsymbol{V} + \boldsymbol{L}^p) \tag{7}$$

which combines transport of the excess density with the evolution $\dot{\boldsymbol{\alpha}} = -\mathrm{curl}\,(\boldsymbol{L}^p)$ implied (but not generally addressed) in classical plasticity, where $\boldsymbol{L}^p$ is the plastic part of the velocity gradient for small deformations (the plastic strain rate produced by the SSD density). In Eq. 7 and the following, $\boldsymbol{\alpha}$ and $\boldsymbol{V}$ refer to space-time averaged quantities. This averaged evolution equation of the excess density implies a continuity condition on a material surface of

discontinuity (Acharya, 2007; Acharya et al., 2008), that takes the form

$$[\![\, \boldsymbol{\alpha} \times \boldsymbol{V} + \boldsymbol{L}^p \,]\!] \times \boldsymbol{n} = \boldsymbol{0} \tag{8}$$

where $\boldsymbol{n}$ is the unit normal to the material surface. Varadhan (2007) and Roy and Acharya (2006) solve Eq. 7 directly as part of the solution of the MFDM equations in a small strain setting. This is a challenging task and more so for large strain applications, where our interest lies. As mentioned previously, classical plasticity suggests $\dot{\boldsymbol{\alpha}} = -\mathrm{curl}\,(\boldsymbol{L}^p)$ for the evolution of the dislocation density—the limiting case of $\boldsymbol{V} = \boldsymbol{0}$, i.e., no transport of the dislocation density. This suggests for plasticity a constraint on $\boldsymbol{L}^p$ (Acharya et al., 2008), i.e.,

$$[\![\, \boldsymbol{L}^p \,]\!] \times \boldsymbol{n} = \boldsymbol{0} \tag{9}$$

which indicates a nonlocal character in the plastic velocity gradient. Specifically, tangential continuity is required of $\boldsymbol{L}^p$.

In the finite deformation case the evolution equation for the dislocation density is

$$\frac{d}{dt}\int_a \boldsymbol{\alpha}\, \boldsymbol{n}_a\, da = -\int_c \left(\boldsymbol{\alpha} \times \boldsymbol{V} + \tilde{\boldsymbol{L}}^p\right) d\boldsymbol{x} \;\Rightarrow\; \mathring{\boldsymbol{\alpha}} = -\mathrm{curl}\left(\boldsymbol{\alpha} \times \boldsymbol{V} + \tilde{\boldsymbol{L}}^p\right) \tag{10}$$

for all area patches a bounded by a curve c in the integral form of the equation, where $\boldsymbol{\alpha}$ is a two-point tensor between the current configuration and the intermediate (lattice) configuration, as defined by Willis (1967), and $\mathring{\boldsymbol{\alpha}} \equiv (\mathrm{div}\,\boldsymbol{v})\,\boldsymbol{\alpha} + \dot{\boldsymbol{\alpha}} - \boldsymbol{\alpha}\,\boldsymbol{L}^T$ is a convected derivative (Fox, 1966; Acharya, 2004; Acharya and Roy, 2006; Acharya, 2007). The two-point tensor $\tilde{\boldsymbol{L}}^p$ is constitutively specified as

$$\tilde{\boldsymbol{L}}^p = \sum_{\kappa} \dot{\gamma}^{\kappa}\, \boldsymbol{b}_o^{\kappa} \otimes \boldsymbol{n}_o^{\kappa}\, \boldsymbol{F}^{e-1} \tag{11}$$

where $\dot{\gamma}^{\kappa}$ is the shear rate for slip system κ, and the slip plane direction and normal are specified in the reference configuration by $\boldsymbol{b}_o^{\kappa}$ and $\boldsymbol{n}_o^{\kappa}$, respectively. It can be shown that in the absence of transport of the dislocation density, i.e. $\boldsymbol{V} = \boldsymbol{0}$, Eqs. 10 and 11 and the multiplicative decomposition yield the equation,

$$\mathrm{curl}\left(\boldsymbol{F}^{e-1}\right) = -\boldsymbol{\alpha}\ . \tag{12}$$

See Appendix B for a proof of this argument. Equation 12 is the fundamental kinematic equation expressing the link between incompatibility of the elastic distortion and the dislocation density tensor (Willis, 1967; Acharya and Bassani, 2000). Equations 10 and 12 indicate that the appropriate continuity requirements in our definition of finite

deformation plasticity, in the case of $\boldsymbol{V} = \boldsymbol{0}$ and $\boldsymbol{F} = \boldsymbol{F}^e\,\boldsymbol{F}^p$, are

$$\left[\!\left[\; \boldsymbol{L}^p\,\boldsymbol{F}^{e-1} \;\right]\!\right] \times \boldsymbol{n} = \boldsymbol{0} \tag{13}$$

$$\left[\!\left[\; \boldsymbol{F}^{e-1} \;\right]\!\right] \times \boldsymbol{n} = \boldsymbol{0} \tag{14}$$

where $\boldsymbol{L}^p = \dot{\boldsymbol{F}}^p\,\boldsymbol{F}^{p-1} := \sum_\kappa \dot{\gamma}^\kappa\,\boldsymbol{b}_o^\kappa \otimes \boldsymbol{n}_o^\kappa$. In the following section we will discuss the implications of this continuity in a finite deformation viscoplastic setting.

3. Continuity of the plastic strain rate and its interpretation in a finite deformation viscoplastic formulation

3.1. Kinematics

In finite deformation elastic-plastic modeling, the multiplicative decomposition of the deformation gradient, $\boldsymbol{F} = \boldsymbol{F}^e\,\boldsymbol{F}^p$, is a classic way to describe the kinematic behavior of a body (Kröner, 1959; Lee and Liu, 1967; Lee, 1969; Kratochvil, 1973), as shown in Fig. 2. The decomposition assumes the existence of an intermediate configuration

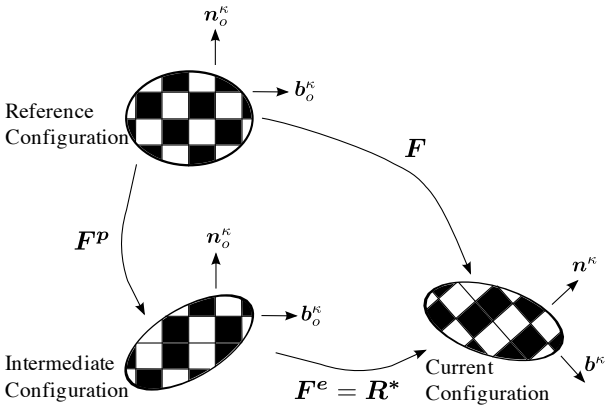

Figure 2: Multiplicative decomposition of the deformation gradient.

obtained through plastic loading of the reference configuration or elastic unloading of the current configuration. A notable assumption is that while the total deformation gradient is required to be derived from a continuous mapping, in general, its component parts have no such requirement and so they inherently become local quantities (Lee, 1969). As Lee (1982) notes, unloading after inhomogeneous plastic flow leaves a body in a state of residual stress because the plastic deformation, the mapping from the reference configuration to the intermediate configuration, when viewed as a mapping of points, is not a continuous, differentiable mapping. Consequently, what we may be left with in the multiplicative decomposition are point-matrix mappings, local tensors describing the motion of infinitesimal neighborhoods. This is a critical point for understanding the general form of plasticity modeling today—the solution of independent ordinary differential equations (ODEs). This will become more clear as we discuss the rate form of the equation. Lee's view of the deformation gradient is appropriate for the bulk material when viewing a continuum point

in a body, but when we view the body at a scale where interfaces such as grain boundaries appear, the continuity requirements stated above augment the multiplicative decomposition with an interface condition.

For simplicity of the ensuing discussion of the continuity constraint, we restrict ourselves to a viscoplastic formulation in which the elastic deformation gradient $\boldsymbol{F}^e$ is equal to the rotation field $\boldsymbol{R}^*$ (a rotation from the orginal lattice to the current lattice configuration). This is a common assumption in large strain metal plasticity where elastic strains are typically two (or more) orders of magnitude less than plastic strains. The velocity gradient follows from the equation

$$\boldsymbol{L} = \dot{\boldsymbol{F}}\,\boldsymbol{F}^{-1} = \dot{\boldsymbol{R}}^*\,\boldsymbol{R}^{*T} + \boldsymbol{R}^*\,\boldsymbol{L}^p\,\boldsymbol{R}^{*T} \tag{15}$$

where the plastic velocity gradient $\boldsymbol{L}^p \equiv \dot{\boldsymbol{F}}^p\,\boldsymbol{F}^{p-1}$. In crystal plasticity the plastic velocity gradient $\boldsymbol{L}^p$ is usually specified through the constitutive relation

$$\boldsymbol{L}^p = \sum_\kappa \dot{\gamma}^\kappa\,\boldsymbol{b}_o^\kappa \otimes \boldsymbol{n}_o^\kappa \tag{16}$$

in which $\dot{\gamma}^\kappa$ is the shear rate for slip system κ, and the slip plane direction and normal are specified in the reference configuration by $\boldsymbol{b}_o^\kappa$ and $\boldsymbol{n}_o^\kappa$, respectively. In a rate-dependent formulation the slip system shear rate is often related to the resolved shear stress τ^κ by a power law of the form

$$\dot{\gamma}^\kappa = \dot{\gamma}_o \left|\frac{\tau^\kappa}{\tau_o}\right|^{1/m} \operatorname{sgn}(\tau^\kappa) \tag{17}$$

where $\dot{\gamma}_o$ is a reference shear rate, τ_o is the slip system strength, and m is the rate sensitivity exponent. Components of the slip system strength evolve with deformation according to specified hardening laws.

We rewrite the equation for the velocity gradient as

$$\boldsymbol{L} = \boldsymbol{\Omega} + \boldsymbol{R}^*\,\boldsymbol{L}^p\,\boldsymbol{R}^{*T} \tag{18}$$

where the lattice spin tensor $\boldsymbol{\Omega} \equiv \dot{\boldsymbol{R}}^*\,\boldsymbol{R}^{*T}$. The velocity gradient is decomposed into its symmetric and skew-symmetric parts as

$$\boldsymbol{D} = \boldsymbol{R}^*\,\boldsymbol{D}^p\,\boldsymbol{R}^{*T} \tag{19}$$

and

$$\boldsymbol{W} = \boldsymbol{\Omega} + \boldsymbol{R}^*\,\boldsymbol{W}^p\,\boldsymbol{R}^{*T}\ . \tag{20}$$

From the definition of $\boldsymbol{\Omega}$ we can write an evolution equation for the lattice rotation field as

$$\dot{\boldsymbol{R}}^* = \boldsymbol{\Omega}\,\boldsymbol{R}^* \tag{21}$$

which is an equation in crystal viscoplasticity that is commonly used to update the rotation field. It is typical to solve

this independent set of ODEs at material points with $\boldsymbol{\Omega} = \boldsymbol{W} - \boldsymbol{R}^{*}\,\boldsymbol{W}^{p}\,\boldsymbol{R}^{*T}$, obtained through the rearrangement of the equation for the skew-symmetric part of the velocity gradient (Eq. 20). We will see that the continuity condition indicates continuity in the lattice rotation field $\boldsymbol{R}^{*}$ and therefore Eq. 21 will become a spatially coupled set of ODEs.

3.2. Continuity

In the finite deformation case and at a material surface of discontinuity, the continuity required by the fundamental equation of incompatibility (Eq. 14) implies the continuity required by the evolution equation for the excess dislocation density (Eq. 13). We can rewrite Eqs. 13 and 14 as

$$\left[\!\left[\, \dot{\boldsymbol{F}}^{p}\,\boldsymbol{F}^{p-1}\,\boldsymbol{F}^{e-1} \times \boldsymbol{n} \,\right]\!\right] = \boldsymbol{0} \tag{22}$$

$$\left[\!\left[\, \boldsymbol{F}^{e-1} \times \boldsymbol{n} \,\right]\!\right] = \boldsymbol{0} \quad , \tag{23}$$

using $\boldsymbol{L}^{p} = \dot{\boldsymbol{F}}^{p}\,\boldsymbol{F}^{p-1}$ and because there is no jump in the normal vector $\boldsymbol{n}$. These conditions can be alternatively stated as

$$\left[\!\left[\, \dot{\boldsymbol{F}}^{p}\,\boldsymbol{F}^{p-1}\,\boldsymbol{F}^{e-1}\,\boldsymbol{t} \,\right]\!\right] = \boldsymbol{0} \tag{24}$$

$$\left[\!\left[\, \boldsymbol{F}^{e-1}\,\boldsymbol{t} \,\right]\!\right] = \boldsymbol{0} \quad , \tag{25}$$

for all tangent vectors $\boldsymbol{t}$ in the interface. Using the definition of the multiplicative decomposition of the deformation gradient, $\boldsymbol{F} = \boldsymbol{F}^{e}\,\boldsymbol{F}^{p}$, we can write

$$\left[\!\left[\, \dot{\boldsymbol{F}}^{p}\,\boldsymbol{F}^{-1}\,\boldsymbol{t} \,\right]\!\right] = \boldsymbol{0} \tag{26}$$

$$\left[\!\left[\, \boldsymbol{F}^{p}\,\boldsymbol{F}^{-1}\,\boldsymbol{t} \,\right]\!\right] = \boldsymbol{0} \quad , \tag{27}$$

or alternatively,

$$\left[\!\left[\, \dot{\boldsymbol{F}}^{p}\,\boldsymbol{t}_{o} \,\right]\!\right] = \left[\!\left[\, \dot{\boldsymbol{F}}^{p} \,\right]\!\right]\boldsymbol{t}_{o} = \boldsymbol{0} \tag{28}$$

$$\left[\!\left[\, \boldsymbol{F}^{p}\,\boldsymbol{t}_{o} \,\right]\!\right] = \left[\!\left[\, \boldsymbol{F}^{p} \,\right]\!\right]\boldsymbol{t}_{o} = \boldsymbol{0} \quad , \tag{29}$$

where $\boldsymbol{t}_{o}$ is the image of $\boldsymbol{t}$ under the inverse deformation gradient. If we take the time derivative of Eq. 29 we get Eq. 28 and therefore the second continuity condition implies the first and vice versa. In our viscoplastic setting

$$\left[\!\left[\, \boldsymbol{F}^{e-1} \,\right]\!\right] \times \boldsymbol{n} = \boldsymbol{0} \;\Rightarrow\; \left[\!\left[\, \boldsymbol{R}^{*T} \,\right]\!\right] \times \boldsymbol{n} = \boldsymbol{0} \tag{30}$$

and

$$\left[\!\left[\, \boldsymbol{R}^{*T} \,\right]\!\right] \times \boldsymbol{n} = \boldsymbol{0} \;\Rightarrow\; \left[\!\left[\, \boldsymbol{R}^{*T} \,\right]\!\right] = \left[\!\left[\, \boldsymbol{R}^{*} \,\right]\!\right] = \boldsymbol{0}\,, \tag{31}$$

i.e. the rotation field is continuous. See Appendix C for a proof of this argument. Since we are talking about a material surface we can also conclude that

$$[\![\, \dot{\boldsymbol{R}}^* \,]\!] = \boldsymbol{0} \,. \tag{32}$$

It is an easy extension to see that Eqs. 31 and 32 imply

$$[\![\, \boldsymbol{\Omega} \,]\!] = [\![\, \dot{\boldsymbol{R}}^* \boldsymbol{R}^{*T} \,]\!] = [\![\, \dot{\boldsymbol{R}}^* \,]\!] \boldsymbol{R}^{*T} = \dot{\boldsymbol{R}}^* [\![\, \boldsymbol{R}^{*T} \,]\!] = \boldsymbol{0} \,. \tag{33}$$

This indicates that the lattice spin is continuous, which will be our constraint for imposing the required continuity in the lattice rotation field. In our computations a grain is composed of one or more finite elements and element interfaces represent a material surface, therefore a continuous rotation field is imposed within a grain in addition to across grain boundaries. Grain neighbor interaction is now inherent in the update of the rotation field.

3.3. Relaxed constraints and co-rotation

Consider an infinite planar material surface in a cartesian coordinate system, as shown in Fig. 3, where the surface is perpendicular to the normal direction. The rolling, transverse and normal directions are designated by R, T, and

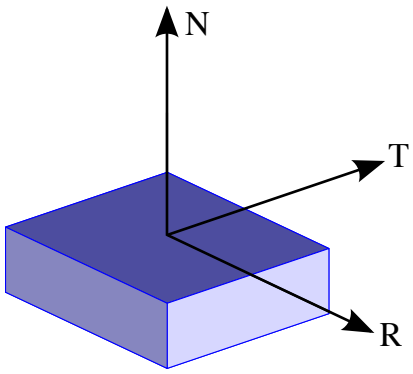

Figure 3: Planar material surface.

N, respectively. We can imagine that if the domain is flattened (flat-grain limit) in the N direction (which means the surface to volume ratio is large) then the deformation constraint is entirely dictated by the boundary. Classical continuum mechanics tells us that we must have a continuous velocity field at the interface to prevent boundary sliding or the body from breaking up. This continuity in the velocity field allows for the trivial satisfaction of tangential continuity in the velocity gradient, i.e. $[\![\, \boldsymbol{L} \,]\!] \times \boldsymbol{n} = \boldsymbol{0}$ is satisfied. If we now write out the 9 components of the resultant tensor and set them equal to zero we obtain $[\![\, L_{RR} \,]\!] = [\![\, L_{TT} \,]\!] = [\![\, L_{RT} \,]\!] = [\![\, L_{TR} \,]\!] = [\![\, L_{NT} \,]\!] = [\![\, L_{NR} \,]\!] = 0$, i.e., these six components of $\boldsymbol{L}$ are constrained on the material surface. The remaining three components (L_{NN}, L_{TN}, L_{RN}) are free, i.e., the jump can take any value. In the following analysis we will refer to components that are constrained to be continuous as constrained and components that are not constrained as free. To satisfy traction continuity in this

case we require $[\![\sigma'_{RN}]\!] = [\![\sigma'_{TN}]\!] = [\![\sigma'_{NN}]\!] = 0$. The quantity $\boldsymbol{R}^* \boldsymbol{L}^p \boldsymbol{R}^{*T}$ is the plastic velocity gradient rotated to the current configuration, and for the purpose of our analysis we define $\boldsymbol{L}^c = \boldsymbol{R}^* \boldsymbol{L}^p \boldsymbol{R}^{*T}$. This allows us to write the velocity gradient as $\boldsymbol{L} = \boldsymbol{\Omega} + \boldsymbol{L}^c$ which means that our continuity condition on the spin field implies the following continuity in the rotated plastic velocity gradient.

$$[\![\boldsymbol{\Omega}]\!] = \boldsymbol{0} \;\Rightarrow\; [\![\boldsymbol{\Omega}]\!] \times \boldsymbol{n} = \boldsymbol{0} \;\Rightarrow\; [\![\boldsymbol{L}^c]\!] \times \boldsymbol{n} = \boldsymbol{0} \tag{34}$$

3.3.1. Relaxed Constraints

The assumptions of the relaxed constraints and LAMEL models are based on the limiting case of flattened grains. These models are not derived from the treatment of a boundary value problem but rather are meant as a way of partitioning the macroscale velocity gradient to the grains in a material point simulation, like in a Taylor model. The relaxed constraints (RC) model, first suggested by Honneff and Mecking (1978) relaxes the out-of-plane shear components of $\boldsymbol{L}$ (by allowing an arbitrary jump in L^c_{TN} and L^c_{RN}) when grains become long and flat, i.e., the surface to volume ratio is large, in order to satisfy traction continuity. The classical RC model treats only a single grain at a time and thus "fully relaxes" the out-of-plane shear components so that the out-of-plane shear stresses are zero, thus trivially satisfying the traction continuity condition specified by continuum mechanics at the interface. The LAMEL model of Van Houtte and co-workers relaxes the same shear components in the grains as the RC model, but theirs is a two-grain model in which the jumps in L^c_{TN} and L^c_{RN} are not arbitrary as in the classical RC model. The velocity gradient of the grains is subject to a minimization of total rate of plastic work which amounts to satisfying the traction continuity condition with non-zero out-of-plane shear stresses. This effectively lessens the relaxation of the L_{TN} and L_{RN} components and has led to better cold rolling texture predictions for steel and aluminum (Van Houtte et al., 1999, 2005). Lee et al. (2002) make the specific requirements of a continuous velocity field and traction continuity across a bicrystal interface. However, all of these models do not specify the continuity which is allowed in the rotated plastic velocity gradient and the spin.

3.3.2. Co-rotation

Co-rotation (or co-spin) models say something more than just velocity and traction continuity required by that of classical continuum mechanics. These models dictate that pairs of grains sharing an interface must maintain constant relative orientation, or that they must co-rotate. In order to co-rotate the grains' lattice spin must be the same. This is similar to our requirement of $[\![\boldsymbol{\Omega}]\!] = \boldsymbol{0}$ at an interface, so in an interface dominated problem (flat-grain limit) the co-rotation model is a good approximation of the continuity condition. Originally proposed by Bolmaro et al. (1997), several variations on this approach are summarized in Tomé et al. (2002). These models can predict textures which are quantitatively closer to experimental results, as discussed in the Introduction.

3.3.3. Continuity in $\boldsymbol{\Omega}$

We can gain further insight into the continuity requirements by decomposing the rotated plastic velocity gradient into its symmetric and skew parts, $\boldsymbol{L}^c = \boldsymbol{D}^c + \boldsymbol{W}^c$. Looking at the diagonal or stretch components first, we see that for the in-plane components $[\![D^c_{RR}]\!] = [\![L^c_{RR}]\!] = 0$ and $[\![D^c_{TT}]\!] = [\![L^c_{TT}]\!] = 0$ and the out-of-plane component D^c_{NN} is free[2]. For the off-diagonal shear components we see that $[\![D^c_{RT}]\!] = [\![D^c_{TR}]\!] = \frac{1}{2}\left([\![L^c_{RT}]\!] + [\![L^c_{TR}]\!]\right) = 0$, and similarly the spin components W^c_{RT} and W^c_{TR} are constrained as well. The analysis for the 'RN' & 'NR' shears and the 'TN' & 'NT' shears are similar, and so we will only discuss the former pair of shears. We have for the symmetric part $[\![D^c_{RN}]\!] = [\![D^c_{NR}]\!] = \frac{1}{2}\left([\![L^c_{RN}]\!] + [\![L^c_{NR}]\!]\right) = \frac{1}{2}[\![L^c_{RN}]\!]$ and for the skew part $[\![W^c_{RN}]\!] = -[\![W^c_{NR}]\!] = \frac{1}{2}\left([\![L^c_{RN}]\!] - [\![L^c_{NR}]\!]\right) = \frac{1}{2}[\![L^c_{RN}]\!]$. These components are free in the sense that they are equal to one-half of the jump in L^c_{RN} which is unconstrained. However, we see that the absolute value of the jump in the skew-symmetric component of $\boldsymbol{L}^c$ is equal to the jump in the corresponding symmetric component, i.e. there is a relationship between the jumps in the symmetric and skew components.

Rewriting Eq. 20 as $\boldsymbol{\Omega} = \boldsymbol{W} - \boldsymbol{W}^c$, we see that by requiring continuity in $\boldsymbol{\Omega}$ we are correcting the rotated plastic spin field, $\boldsymbol{W}^c$, to satisfy the required continuity in $\boldsymbol{L}^c$. In a finite element model, a continuous velocity field and traction continuity come as a natural result of the formulation. For a rigid crystal viscoplastic material model, $\boldsymbol{D} = \boldsymbol{D}^c$, and so the continuity required of the symmetric part of the rotated plastic velocity gradient follows from the finite element solution, but a correction of the skew-symmetric part is needed to satisfy the continuity constraint. We detail our method for implementing this correction in the following section.

4. Method

4.1. Hybrid finite element model

For a viscoplastic flow we must satisfy the balance of linear momentum resulting in the equilibrium equation (neglecting body force)

$$\operatorname{div} \boldsymbol{\sigma} = \boldsymbol{0} \tag{35}$$

where $\boldsymbol{\sigma}$ is the Cauchy stress, and the mass balance resulting in the incompressibility constraint

$$\operatorname{div} \boldsymbol{u} = 0 \tag{36}$$

where $\boldsymbol{u}$ is the velocity field. Direct parameterization of the weighted residuals of these equations results in a poorly conditioned system of equations. As an alternative to Eq. 36 we follow Beaudoin et al. (1994) and specify an alternative constraint

$$-\lambda_e \operatorname{div} \boldsymbol{u} = \Delta p \tag{37}$$

[2]However, in the viscoplastic setting D^c_{NN} would be constrained due to the incompressibility constraint.

where $\lambda_e = \alpha\,\mu_e$ is the product of a fixed scaling parameter α and a parameter μ_e, which depends on the individual element constitutive response. The pressure is taken as constant in an element. This alternative constraint (due to Zienkiewicz et al. (1985)) effectively decouples the iterative matrix solution from the incompressibility constraint and therefore α need not be very large as in a traditional penalty method. As the pressure p converges, incompressibility is satisfied.

From Eq. 35 we have the usual residual resulting from equilibrium

$$\mathcal{R}_e\left(\boldsymbol{u}\right) = \int_{\mathcal{B}_e} \mathrm{tr}\left(\boldsymbol{\sigma}' \cdot \mathrm{grad}\,\boldsymbol{\phi}\right) dV - \int_{\mathcal{B}_e} p\ \mathrm{div}\,\boldsymbol{\phi}\ dV - \int_{\partial\mathcal{B}_t} \boldsymbol{\phi} \cdot \boldsymbol{t}\ dV = 0 \tag{38}$$

where $\boldsymbol{\phi}$ is a weighting function on the velocity field $\boldsymbol{u}$, $\mathcal{B}_e$ is the element volume, $\partial\mathcal{B}_t$ is the element boundary where tractions $\boldsymbol{t}$ are specified and a sum over elements is implied. Equation 37 results in a residual on the velocity and pressure fields

$$\mathcal{R}_p\left(\boldsymbol{u}, p\right) = \int_{\mathcal{B}_e} \psi \left(\mathrm{div}\,\boldsymbol{u} + \frac{1}{\lambda_e}\Delta p\right)\ dV = 0 \tag{39}$$

where ψ is a weighting function on the pressure field. The hybrid finite element code follows that of Beaudoin et al. (1995) and it is dependent upon the previously stated residuals in addition to a residual for the crystal constitutive response, given by

$$\mathcal{R}_s\left(\boldsymbol{\sigma}'\right) = \int_{\mathcal{B}_e} \boldsymbol{\Psi} : \left(\mathcal{P} : \boldsymbol{\sigma}' - \boldsymbol{D}'\right)\ dV = 0 \tag{40}$$

where $\boldsymbol{\Psi}$ are weighting functions on the deviatoric stress, $\mathcal{P}$ is the crystal constitutive response matrix and $\boldsymbol{D}'$ is the deviatoric part of the deformation rate. The hybrid method results in an increase in computational cost versus a standard velocity-pressure formulation (due to parameterization of the deviatoric stress) but allows for the elimination of the stress term from the equilibrium residual with the stress solved for from the constitutive residual. This smoothes the constitutive response and convergence is more likely for problems with considerable plastic anisotropy, e.g., a polycrystal discretized by one or more elements per grain—which is the case for all simulations herein.

The solution procedure closely mimics Eggert et al. (1991) in which derivatives are computed for the equilibrium and pressure residuals with respect to the unknowns, $\boldsymbol{u}$ and p. This results in matrix equations for the incremental velocity and pressure. The velocity and spin fields are solved for on a mesh of hexahedral elements with linear shape functions and the pressure field is constant in an element. The code utilizes the Matlab Parallel Computing Toolbox (The Mathworks, Inc., 2008) by running element loops in parallel on multiple "worker" sessions of Matlab, which are controlled by a client session that handles all serial computation such as initialization, matrix solve, and output.

4.2. Enforcing the continuity constraint

A simple explicit update is used for all state variables including the lattice rotation field. Therefore, at the end of a time step we enforce the continuity of $\boldsymbol{\Omega}$ prior to updating $\boldsymbol{R}^*$. This is accomplished by forming a least squares (LS)

residual on the element volume for the unknown field $\tilde{\boldsymbol{\Omega}}$ as

$$\mathcal{R}_{LS}\left(\tilde{\boldsymbol{\Omega}}\right) = \int_{\mathcal{B}_e} \left(\tilde{\boldsymbol{\Omega}} - \boldsymbol{\Omega}\right)^2 dV \tag{41}$$

where $\boldsymbol{\Omega} = \boldsymbol{W} - \boldsymbol{R}^* \boldsymbol{W}^p \boldsymbol{R}^{*T}$ and a sum over elements is implied. Taking the first variation of the LS residual and setting this equal to zero we obtain

$$\mathcal{R}_{\Omega}\left(\tilde{\boldsymbol{\Omega}}\right) = \int_{\mathcal{B}_e} \delta\tilde{\boldsymbol{\Omega}} : \left(\tilde{\boldsymbol{\Omega}} - \boldsymbol{\Omega}\right) dV = 0 \, . \tag{42}$$

Writing the skew-symmetric tensors in Eq. 42 in terms of their corresponding axial vectors (e.g., $\Omega_{ij} = -e_{ijk}\,\omega_k$) we can simplify to the following vector form of the residual statement.

$$\int_{\mathcal{B}_e} \delta\tilde{\boldsymbol{\omega}} \cdot (\tilde{\boldsymbol{\omega}} - \boldsymbol{\omega})\, dV = 0 \tag{43}$$

We introduce basis functions $\boldsymbol{N}^{\boldsymbol{u}}$ for the axial vectors $\delta\tilde{\boldsymbol{\omega}}$ and $\tilde{\boldsymbol{\omega}}$ which leaves us with a linear system of equations to solve for $\tilde{\boldsymbol{\Omega}}$ with a left-hand side that resembles a mass matrix—a system efficiently solved with any direct or iterative solver. The rotation field is updated by solving Eq. 21 with the exponential map, i.e.,

$${}^{t+\Delta t}\boldsymbol{R}^* = \exp\left(\tilde{\boldsymbol{\Omega}}\,\Delta t\right) {}^{t}\boldsymbol{R}^* \, . \tag{44}$$

where the continuous field $\tilde{\boldsymbol{\Omega}}$ has been substituted for $\boldsymbol{\Omega}$, and t and $t + \Delta t$ represent the previous and current time steps, respectively.

5. Results & Discussion

5.1. Rolling of a polycrystal

We use plane strain compression to simulate the idealized rolling of an fcc polycrystal composed of 600 grains arranged in a 10 x 10 x 6 (R x T x N) aggregate as shown in Fig. 4(a). The outer layer of grains transmits the boundary conditions to an inner aggregate of 256 (8 x 8 x 4) grains, which are used for our analysis. Each grain is composed of 16 elements arranged so that elements are approximately cubic in shape at 50% reduction ($\epsilon \approx 0.69$), which is shown in Fig. 4(b). Material properties are that of room temperature Cu and the applied strain rate is 1 s^{-1} with a constant time step of $\Delta t = 0.005$ s. Simulations with and without the constraint on the $\boldsymbol{\Omega}$ field were run to 73% reduction ($\epsilon \approx 1.3$). The finite element simulations resulting from the classical update for the rotation field are referred to as 'local' and the constrained as 'nonlocal'. These simulations are compared to a Taylor material point simulation of the 256 orientations in the inner aggregate.

There is much literature dealing with rolling textures of f.c.c. metals and we present the textures in this work as a qualitative measure of the validity of the continuity constraint derived herein. We accomplish this by pointing out

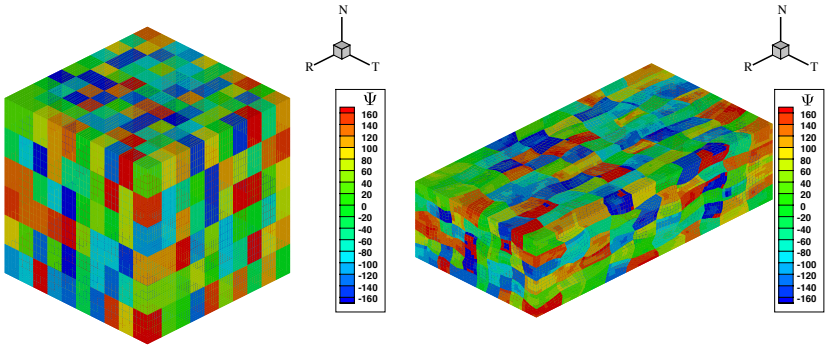

(a) Initial arrangement (b) 50% reduction

Figure 4: Arrangement of the aggregate of 600 f.c.c. grains used in rolling simulation.

differences amongst the simulated textures, especially where established experimental observations suggest our results to be viable. Orientation distribution functions (ODFs) were created from the Euler angles of the inner aggregate using software from the DPLAB Polycrystal Library at Cornell (Dawson et al., 2008). Figures 5 and 6 show the ODFs plotted on (111) and (100) pole figures at true strain levels of 0.69 and 1.3, respectively. A notable difference in these texture results is the overall weaker texture from the nonlocal simulation relative to the local and Taylor simulations, which is consistent with experimental evidence. Bolmaro et al. (2000) found that a co-spin material point simulation resulted in a close correlation with the experimental texture and a maximum intensity approximately six times less than a simulation without co-spin. The intensity in our nonlocal result is consistent with their findings and the texture is more uniform with a more realistic β fiber (Brass - S - Copper). We can better observe this trend by looking at the ODFs plotted on the cubic fundamental region of Rodrigues' space. This is an axis-angle parameterization in which the axis of rotation is scaled by a function of the angle of rotation. The authors refer the reader to work by Kumar and Dawson (2000) for further information regarding deformation textures over Rodrigues' space for f.c.c. metals.

As deformation increases, the tendency in the Taylor and local models is for the Brass and S components of the β fiber to decrease relative to the increase in the Copper (or Taylor) component. Figures 7 and 8 show the ODFs plotted on the cubic fundamental region (FR) of Rodrigues' space at true strain levels of 0.69 and 1.3 respectively. All of the components except Cube and S are visible on the surface of the FR (plots on left hand side). The right hand side plots show slices through the FR at components in the β fiber. The intensity scales are different for each result so that we can show the uniformity of the nonlocal texture relative to the local and Taylor results. In addition this confirms the weaker intensity for the nonlocal solution, as shown in the pole figure results. At 50% reduction the local and nonlocal solutions show a more uniform and stronger β fiber relative to the Taylor solution. This difference is expected, as local gradients in the finite element solution deviate from the applied deformation rate in the Taylor material point simulation. The nonlocal result has stronger Brass and S components relative to the Copper/Taylor components than the local result and this difference is maintained at the larger reduction of 73%. At this larger

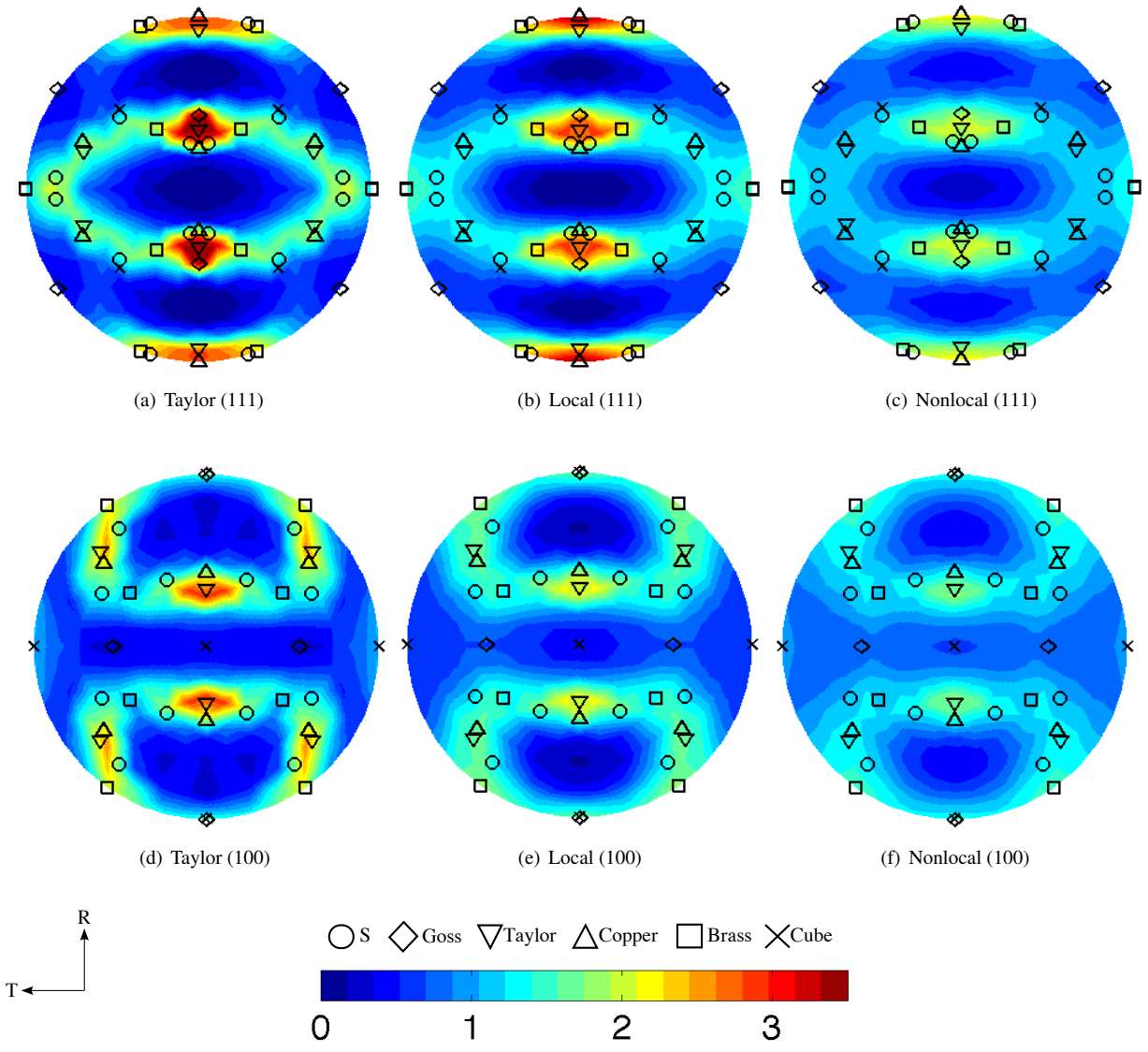

(a) Taylor (111) (b) Local (111) (c) Nonlocal (111)

(d) Taylor (100) (e) Local (100) (f) Nonlocal (100)

Figure 5: ODFs of rolling textures at 50% reduction ($\epsilon \approx 0.69$) plotted on (111) and (100) pole figures for the Taylor, local and nonlocal simulations.

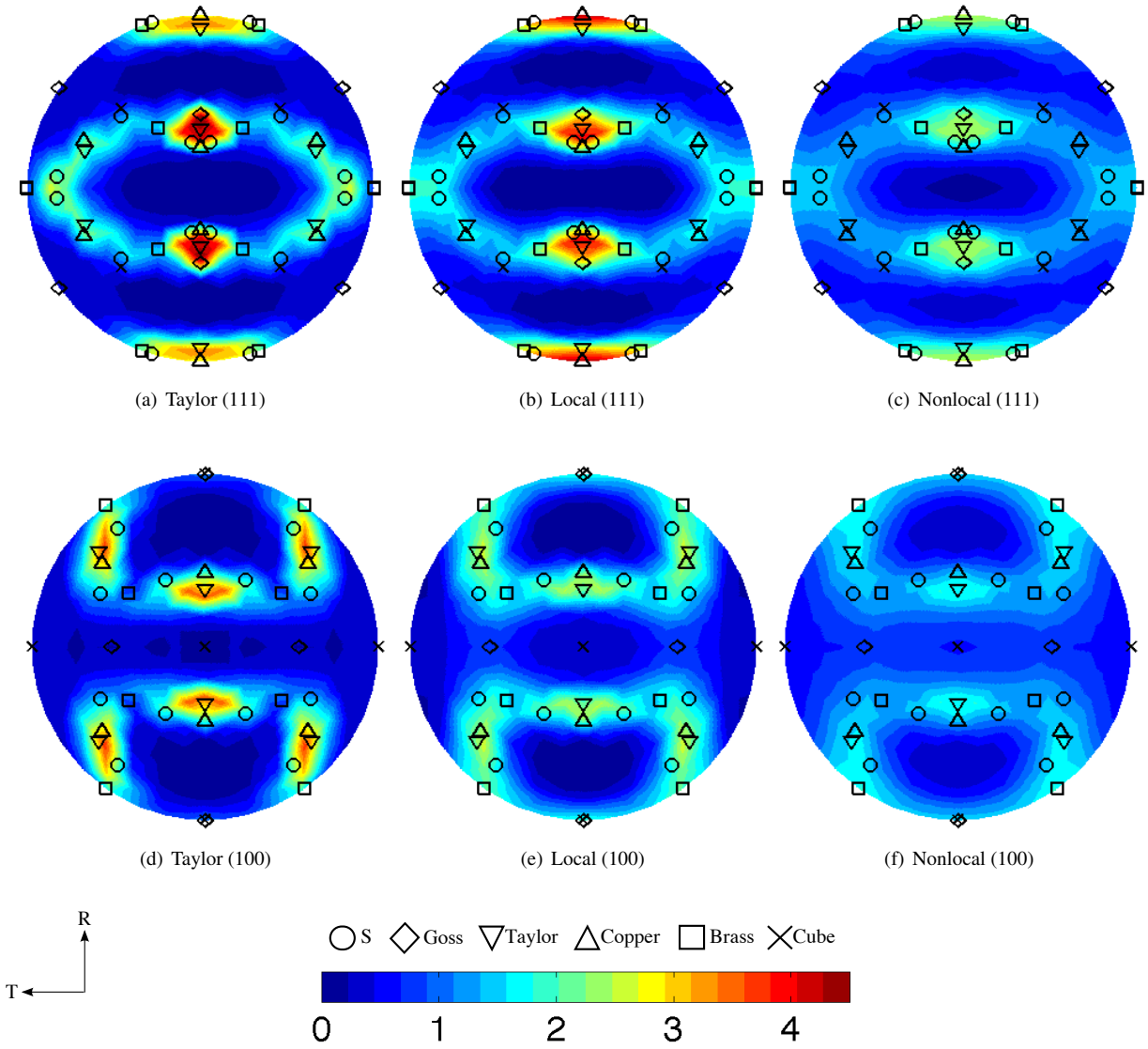

(a) Taylor (111) (b) Local (111) (c) Nonlocal (111)

(d) Taylor (100) (e) Local (100) (f) Nonlocal (100)

Figure 6: ODFs of rolling textures at 73% reduction ($\epsilon \approx 1.3$) plotted on (111) and (100) pole figures for the Taylor, local and nonlocal simulations.

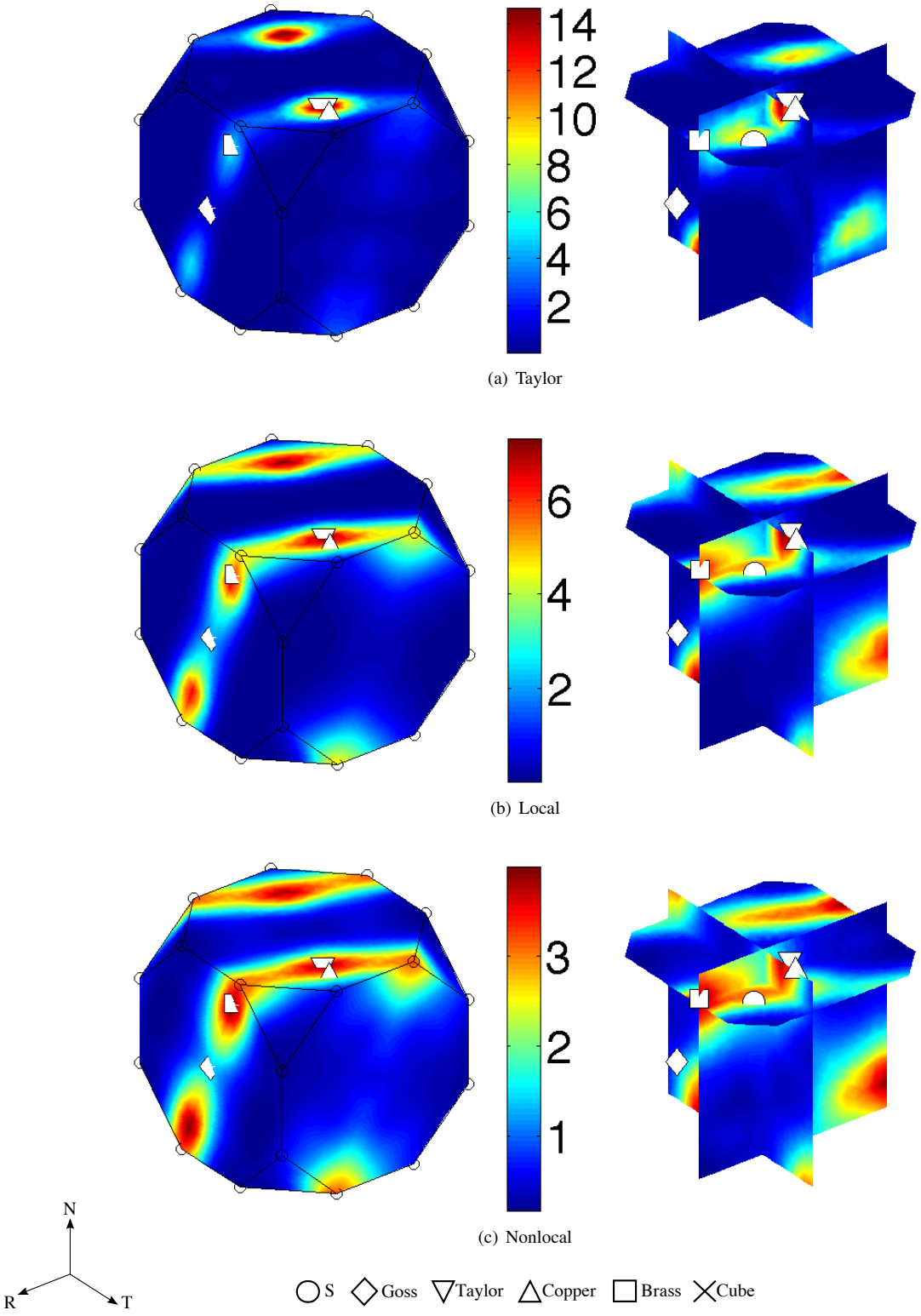

(a) Taylor

(b) Local

(c) Nonlocal

Figure 7: ODFs of rolling textures at 50% reduction ($\epsilon \approx 0.69$) plotted on cubic fundamental region of Rodrigues' space for the Taylor, local and nonlocal simulations.

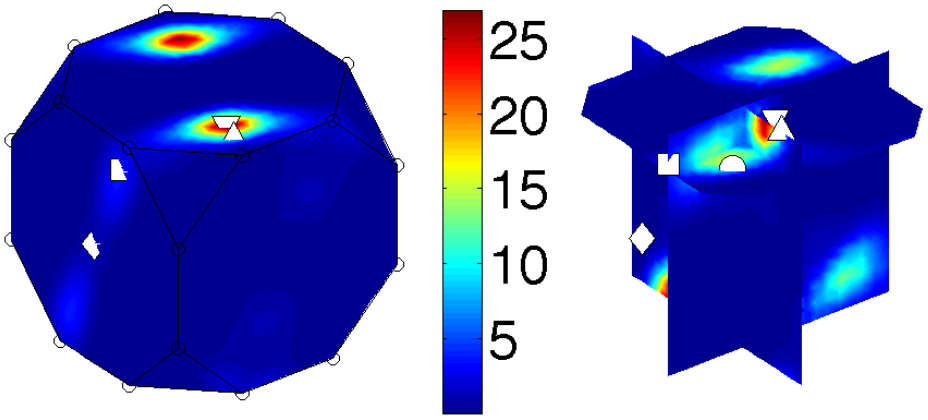

(a) Taylor

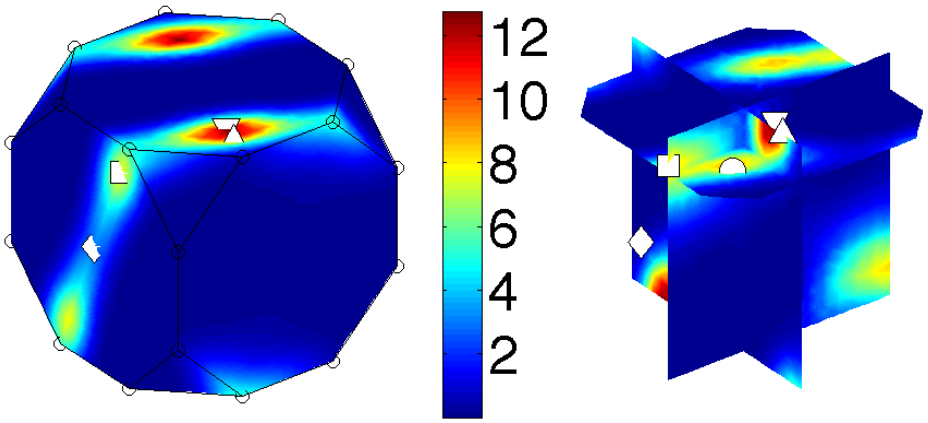

(b) Local

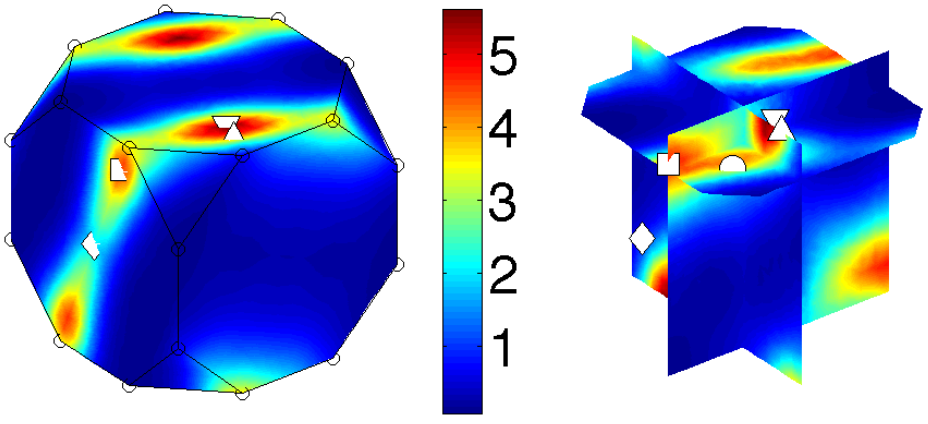

(c) Nonlocal

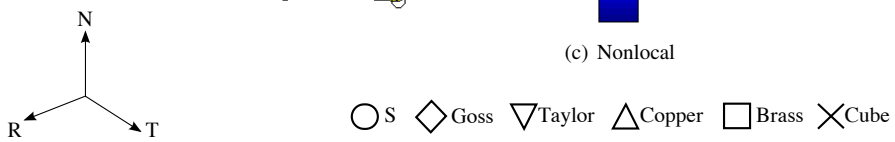

Figure 8: ODFs of rolling textures at 73% reduction ($\epsilon \approx 1.3$) plotted on cubic fundamental region of Rodrigues' space for the Taylor, local and nonlocal simulations.

reduction the β fiber begins to disappear altogether for the Taylor result and weakens greatly for the local result, while the nonlocal result shows a much stronger and more even fiber. For experimental support of these results the reader is referred to the comprehensive work of Hirsch and Lücke (1988).

5.2. Lattice rotations of individual grains

Current high energy X-ray diffraction techniques allow the observation of *in situ* lattice rotations of individual grains in a bulk sample. An exceptional example of this is the work of Winther et al. (2004), in which the lattice rotations of aluminum grains are tracked under uniaxial tensile deformation of a bulk sample to 6% strain. Figure 9 shows Winther's observed lattice rotations for eight grains, plotted on an inverse pole figure. The lines connecting

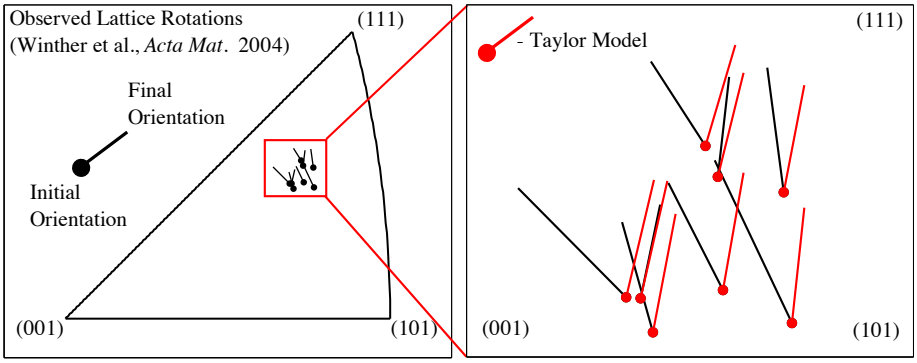

Figure 9: Observed lattice rotations plotted with result from Taylor model (Winther et al., 2004).

initial and final orientations in Fig. 9 indicate direction only and not the entire orientation evolution path. This region of orientation space is chosen because of the discrepancies in the experimental data and differences from the Taylor material point simulation results. The majority of grains in this region rotate towards the (001)-(111) line, but a few are closer to the Taylor direction of rotation, i.e., towards the (111) direction. It is important to note that spatial information in these experiments is unknown, i.e., the portion of the grain which rotates in the observed direction is unkown.

As it is difficult to know the precise grain shape and orientation neighborhood in the experiments, we propose a finite element simulation which serves as a constrained limit to the actual grain deformation state, and effectively isolates the effect of the continuity constraint. We enforce velocity boundary conditions which mimic that of the Taylor uniaxial tension material point simulation, as shown in Fig. 10. This requires a multi-point constraint on the 'X' and 'Y' faces of the grain such that satisfaction of the incompressibility constraint causes the deformation rate on these faces to be equal to one half of the loading rate on the 'Z' face of the grain. In reality the grain does not experience this constrained deformation state, however, this ensures us that any deviation from a "Taylor" rotation is due solely to the constraint on the spin field. It is certainly possible to adjust the applied deformation rate through the velocity boundary conditions and obtain a rotation towards the (001)-(111) direction, but attempting to match the

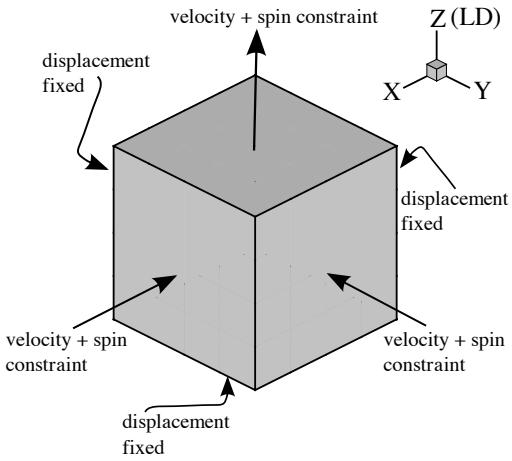

Figure 10: Boundary conditions for single grain (Taylor) finite element simulations.

strain state of the grain would confound the result of the constraint on the spin. To this end, we choose an arbitrary constraint on the spin field by setting the tangential components to zero on all faces of the grain, e.g., on the 'Z' faces the $\tilde{\omega}_x$ and $\tilde{\omega}_y$ components are set to zero—$\tilde{\boldsymbol{\omega}}$ is the axial vector of the continuous spin field $\tilde{\boldsymbol{\Omega}}$. Similar results are obtained when the normal component is constrained rather than the tangential components.

It was found that a mesh of 4 x 4 x 4 elements captures the general trend in the lattice rotations. Figure 11 shows the simulated lattice rotations of all the grains studied (subject to the spin constraint discussed previously), plotted with Winther's observed rotations and the result from the Taylor model. A blue dot is an orientation at a material point in the grain, an integration point, in the case of a finite element model. The first thing to note is that the average simulated rotations is approximately in the direction of the Taylor model. This is to be expected since the strict velocity boundary conditions in the finite element model mimic the Taylor material point simulation. However, the average rotation is less than the Taylor model while local rotations tend to be larger. This is consistent with the result of the rolling textures, in which overall intensity was less while some components were stronger relative to other components. Several of the grains exhibit a splitting phenomenon in which a portion of the grain rotates in the (001)-(111) direction observed by Winther et al. (2004), e.g., grains G2-3 and G6-8. This is a significant result because the constraint on the spin field on the boundary of the grain is the only factor affecting the lattice orientation from rotating in the Taylor direction. It is conceivable that the grain neighborhood would have a similar effect at grain boundaries in real materials. The authors acknowledge that other factors such as the grain deformation state and grain shape affect the lattice rotation in a significant manner, however, the point here is to isolate the effect of the continuity condition. It is reasonable and experimentally observed that grains split and rotate in several directions, see for example the work of Wert and Thorning (2005). Although orientation spread was observed in the local model, there was no distinct splitting as in the nonlocal model (cf. Fig. 12). As a check of the nonlocal model, the local model was run with the spin field constrained for the integration points near the external surfaces of the grain. Since the rotation update is

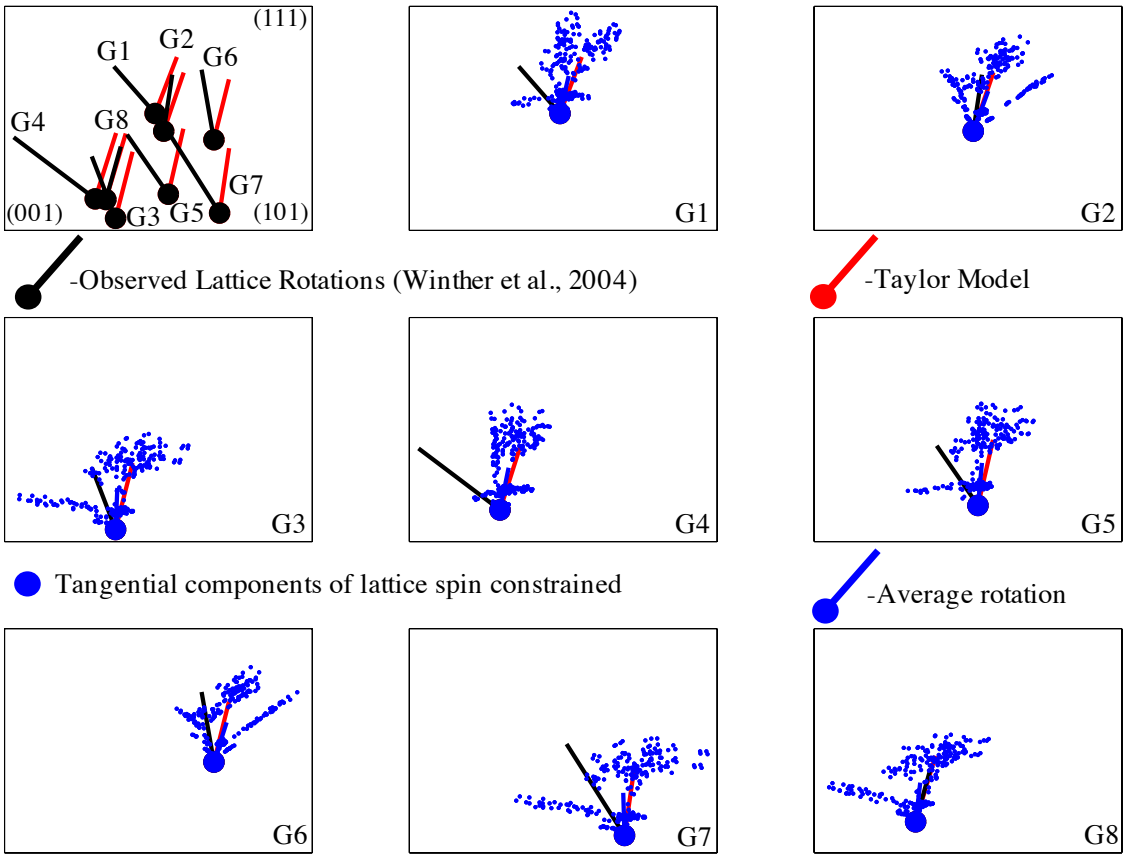

Figure 11: Observed and simulated single grain lattice rotations.

independent at integration points for the local model, the rotations near the surfaces were split away from the Taylor direction as in the nonlocal model, but the rotation directions were not the same as the nonlocal model. The nonlocal model provides a different solution than this altered local solution.

Figure 12 is a detailed plot of the result for grain G2 with the orientations divided into regions 0, 1, 2, and 3. For

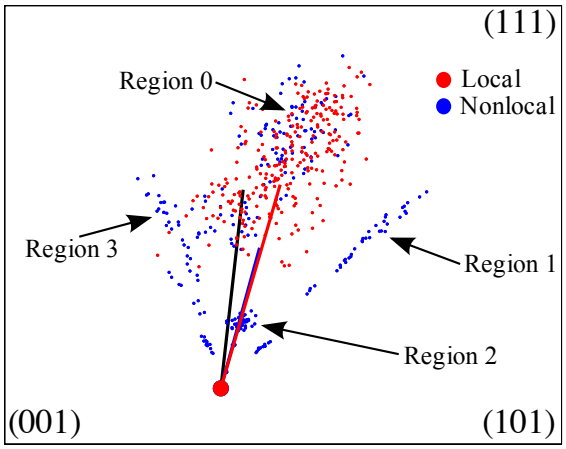

Figure 12: Observed and simulated lattice rotations for grain G2 (cf. Fig 11).

the local treatment of rotation, lattice reorientation mostly follows that of the Taylor model prediction. An average rotation in each of the regions for the nonlocal result was calculated and plotted on a finite element mesh, where each element represents an orientation at one integration point. This is shown in Fig. 13 where the the surface and slices through the center of the grain are shown.

It is appropriate here to discuss the issue of mesh refinement. The simulation for grain G2 was run for finer mesh sizes and although there is more spread in the orientations, the general trends are the same. The average rotation is in the Taylor direction with locally larger rotations and distinct regions are less apparent but rotations in the experimentally observed direction are still evident. A comprehensive mesh refinement study for the rolling texture or S array problems is computationally prohibitive for the current Matlab code, however, refinement for the single grain simulation is presented here. It is the authors' hope that these results can provide some qualitative sense of 'weak' convergence that one might look for in such a highly nonlinear problem. Figure 14 shows the nonlocal result of the mesh refinement study for grain G2 for three different mesh sizes: 4 x 4 x 4, 8 x 8 x 8, and 16 x 16 x 16. Contour lines with an arbitrary log scale for each mesh result are plotted with the orientations, i.e. the three colors represent the scale $c * [0.01\ 0.1\ 1]$ where c is an arbitrary constant which is the same for each plot. The trends are similar for the different mesh sizes, at least in direction of orientation evolution. This 'invariant' character of the texture evolution is further indication that it is the structure of the boundary value problem inherent to the non-local formulation which is at play, and results are not a consequence of numerical treatment—such as the level of mesh refinement

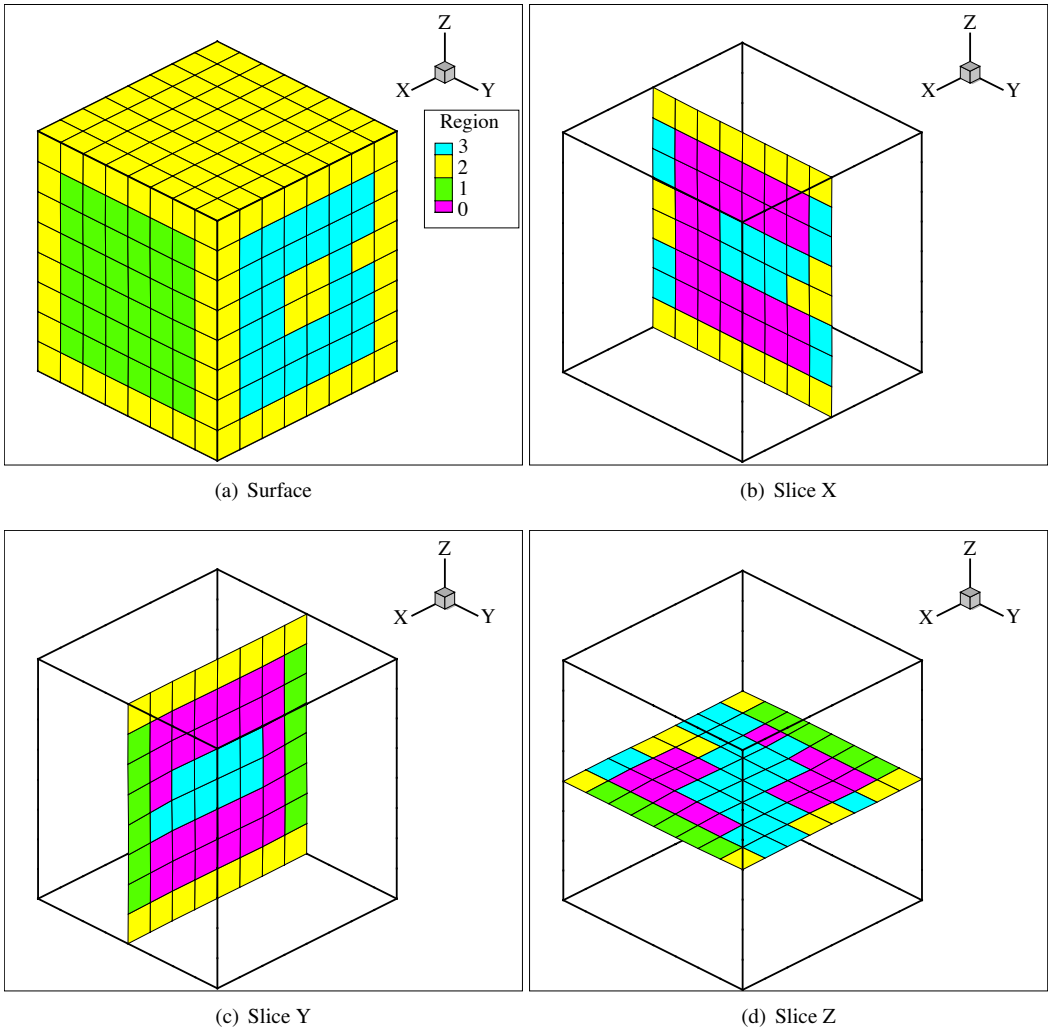

(a) Surface (b) Slice X

(c) Slice Y (d) Slice Z

Figure 13: Grain G2 subdivided into lattice rotation regions.

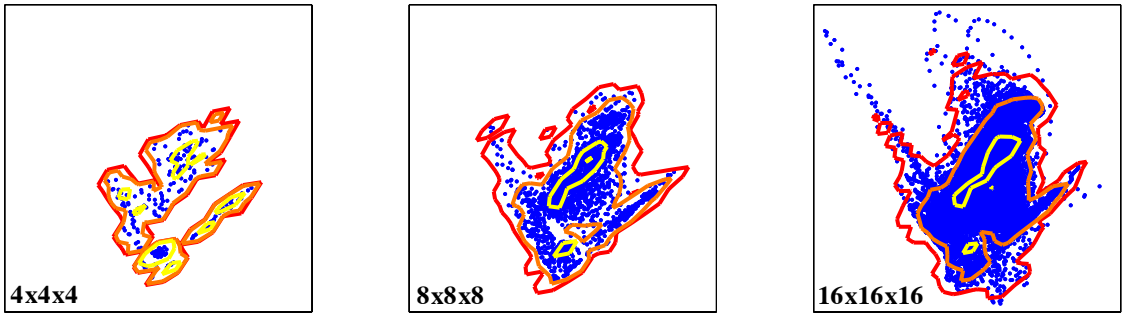

Figure 14: Nonlocal result for grain G2 for three mesh sizes (contour lines are arbitrary log scale).

5.3. Plane strain compression of S orientations

Beaudoin et al. (1996) simulate the idealized rolling of an array of S orientations which are discretized by thousands of finite elements. They find at large strains that localized orientation gradients cause the development of a complete rolling texture from two S orientations. They observed N-rotated cube oriented grains after large deformations, which are associated with recrystallization nuclei in rolling. Our nonlocal simulation results reveal the development of an organized band of N-rotated cube orientations surrounded by defect structure near the grain boundary. Because of the symmetry in the deformation modes of the S orientations, only two grains are needed to represent a three dimensional periodic array of S orientations. Due to the simple geometry and single grain boundary, we choose this model problem to further understand the effect of the continuity constraint at a grain boundary and in the interior of the grain. The geometry of the model is the same as in the work of Beaudoin et al. (1996) where the intial aspect ratio is 4:1:1 (R:T:N), and the upper half of the cube is initialized with the S orientation (-31,37,27) and the lower half with the S orientation (31,143,-153), where the Euler angles are given in Kocks' format. The two grains have opposing 'RN' and 'TN' shear modes.

Cube orientations may serve as recrystallization nuclei when surrounded by a region of high misorientation that provides a driving force for recrystallization. This driving force is related to the stored energy due to the dislocation density field. To this effect a gradient hardening model (Beaudoin et al., 2000; Acharya and Beaudoin, 2000; Beaudoin and Acharya, 2001; Kok et al., 2002) based on a measure of the $\boldsymbol{\alpha}$ tensor is included in the S array simulations to include this gradient effect in the solution of the boundary value problem.

Figure 15 shows the plots of the angle part of an axis-angle representation of the rotation field measured from a cube orientation at a 72% reduction for the local and nonlocal simulations. The thick black line in the figures represents the grain boundary. A cell in these plots represents a single integration point, i.e. four cells is the surface of an element. The rotation from cube is the (minimum) angle part of an axis-angle representation of the misorientation of the integration point orientation with respect to all variants of the cube orientation. At this reduction an organized band of N-direction (N-D) rotated cube orientations was identified along the grain boundary in the upper grain as indicated in Fig. 15(b). The local simulation displayed no such band at this reduction, but some orientations near N-D rotated cube could be found. Beaudoin et al. (1996) identified N-D rotated cube orientations at a larger reduction of 85% at or near the grain boundary in less organized structures. The fact that the N-D rotated cube orientations appear earlier in the deformation and in such an organized structure near the grain boundary indicates that the continuity constraint may play a significant role in the development of this orientation.

To investigate the appearance of the N-D rotated cube orientations further we will look at an effective measure of the excess dislocation density tensor, $\alpha_{\text{eff}} = \sqrt{\boldsymbol{\alpha} : \boldsymbol{\alpha}}$. Figure 16 depicts α_{eff} for the local and nonlocal simulations. One major difference in the results is the higher α_{eff} content in the upper grain near the grain boundary for the nonlocal simulation while little or none exists in the local result. This higher α_{eff} content is in the region where the N-D rotated cube orientations were observed. As the cube orientation is associated with recrystallization nuclei in rolling it is possible that this excess dislocation density could provide the stored energy necessary for recrystallization near the

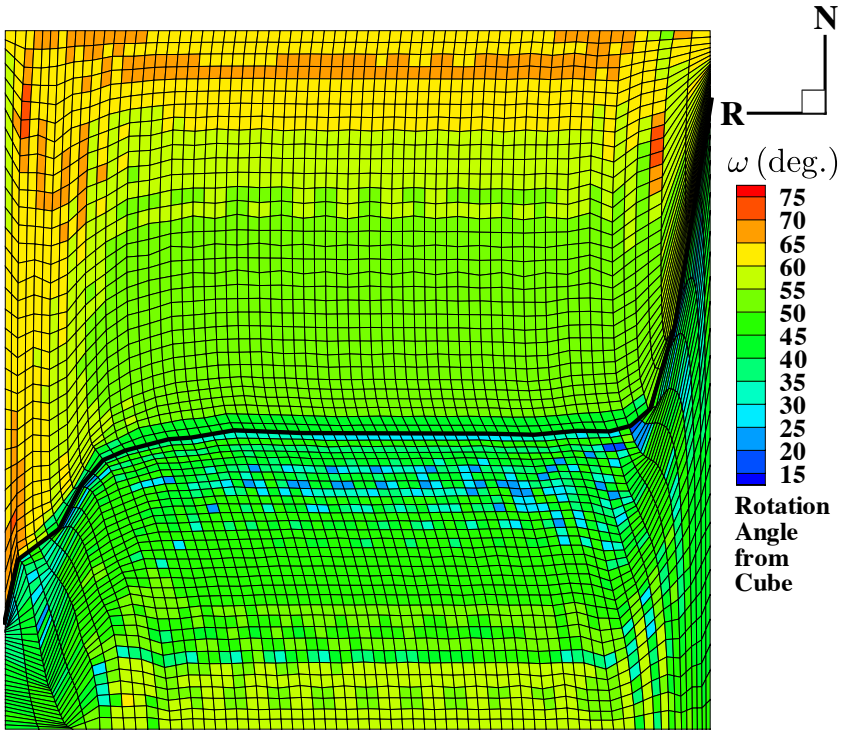

(a) Local

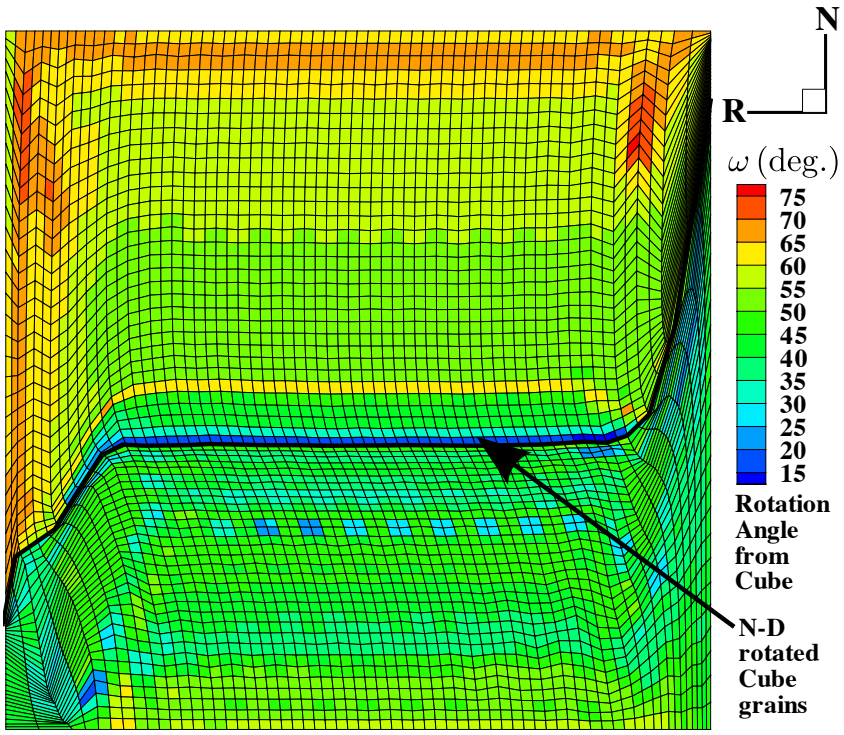

(b) Nonlocal

Figure 15: Rotation angle (from a cube orientation) at the edge of the grains for local and nonlocal simulations of the S array at 72% reduction. The images are scaled by a factor of 50 in the N direction. The initial aspect ratio was 4:1:1 (R:T:N).

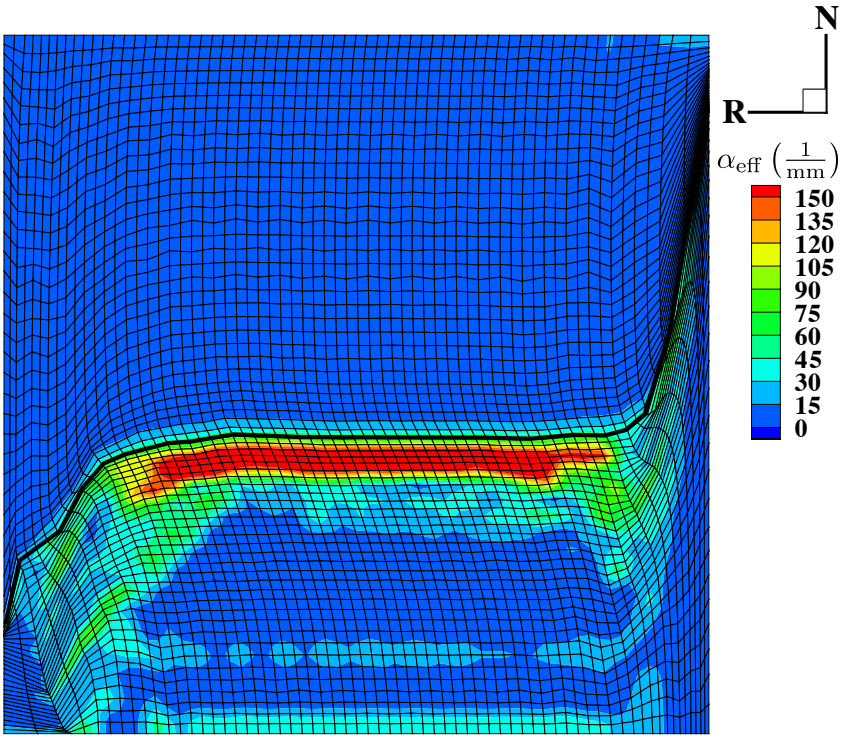

(a) Local

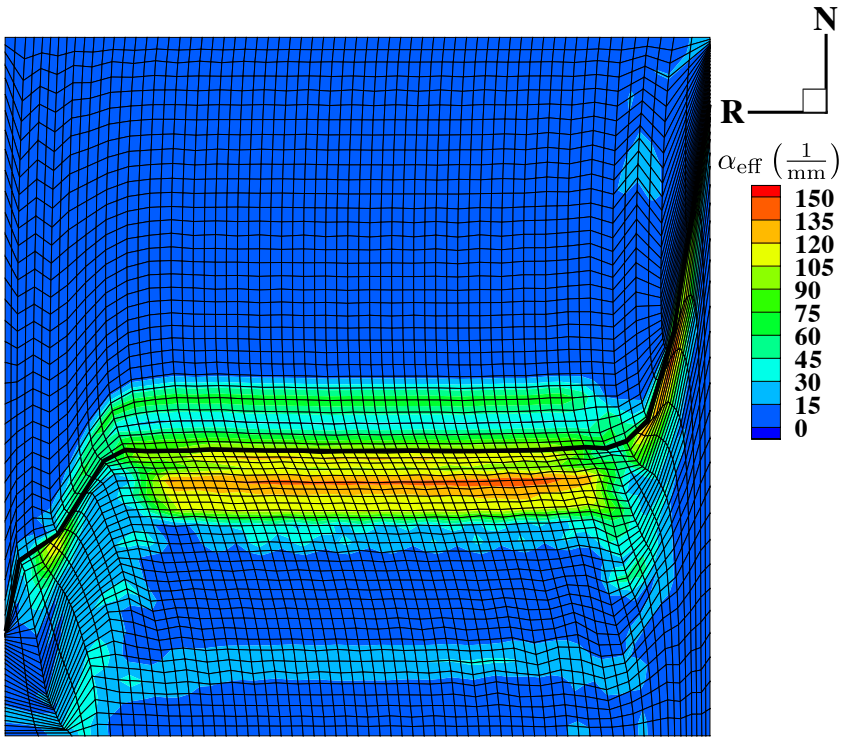

(b) Nonlocal

Figure 16: Effective excess dislocation density ($\alpha_{\text{eff}} = \sqrt{\boldsymbol{\alpha} : \boldsymbol{\alpha}}$) at the edge of the grains for local and nonlocal simulations of the S array at 72% reduction. The images are scaled by a factor of 50 in the N direction. The initial aspect ratio was 4:1:1 (R:T:N).

N-D rotated cube sites. The dominant dislocation density components in these results are those with a line direction into the page (T), i.e. the α_{xT} components, where $x = R, T, N$. Figures 17(a) and 17(b) plot (for the nonlocal case) the magnitude of this vector, $\|\alpha_{xT}\|_2 = \sqrt{\alpha_{RT}^2 + \alpha_{TT}^2 + \alpha_{NT}^2}$, as contours and Fig. 17(b) also depicts arrows which indicate direction (not magnitude) of the resulting Burgers vector. The contour scale is the same as that in Fig. 16(b), which reveals the dominance of these components. The contours of $\|\alpha_{xT}\|_2$ indicate that the maximum is developing at a location removed from the grain boundary in the lower grain. The zoomed picture in Fig. 17(b) shows three rows of direction vectors in this region of maximum $\|\alpha_{xT}\|_2$ pointing in the N direction, i.e. an $\alpha_{NT}\, \boldsymbol{e}_N \otimes \boldsymbol{e}_T$ (Burgers vector $\otimes$ line direction) dominant structure approximately two to three elements from the grain boundary. This suggests a tilt boundary is developing in the immediate vicinity of but removed from the grain boundary. In addition there appear to be oscillations in the direction vector at the level of the mesh surrounding the tilt boundary (alternating pairs of N and -N pointing vectors), however due to the smaller contour magnitude in these regions the authors believe that the dominant structure which is developing is the α_{NT} tilt boundary. Kysar et al. (2007) calculate the Nye tensor using lattice rotations from electron backscatter diffraction (EBSD) measurements of wedge indented f.c.c. single crystals. A similar technique might be used to interrogate the excess density near grain boundaries after severe plastic deformation to see what kind of dislocation structure exists. It is important to note that the initial geometry of a grain is 4 x 0.5 x 0.5 mm (R x T x N) with 32 x 16 x 16 = 8192 elements per grain and so the initial element size is 125 x 31.25 x 31.25 μm. The grain and element sizes are rather large compared with the physical length scale of the gradient hardening model and therefore the a study of such oscillations with mesh refinement and domain size changes is important for future work.

6. Conclusions

Starting from an averaged theory of field dislocation mechanics (MFDM) we have detailed a continuity condition on the constitutively specified plastic velocity gradient. In a finite deformation crystal rigid viscoplastic setting this continuity translates to a constraint on the lattice rotation field, i.e. that this field should be continuous at material surfaces of discontinuity. This condition is consistent with co-rotation type models of crystal plasticity. We have tested the validity of this constraint through texture analysis of rolling simulations for f.c.c. metals. These simulations result in a weaker overall texture and a β fiber which is more consistent with experimental observation than the local and Taylor models. We isolated the effect of the constraint condition through a "Taylor" finite element simulation in which we observed grain splitting—parts of a grain affected by the constraint rotate in the experimentally observed direction. The nonlocal rolling simulations of two S-type orientations produced N-direction rotated cube orientations (associated with recrystallization) earlier in the deformation and in a more organized structure compared to the local result and that of Beaudoin et al. (1996). Also the band of cube orientations was surrounded by defect structures including a tilt boundary in the vicinity of but removed from the grain boundary. In this simulation we have demonstrated the possibility of predicting continuous fields of lattice rotations with sharp gradients representing non-singular

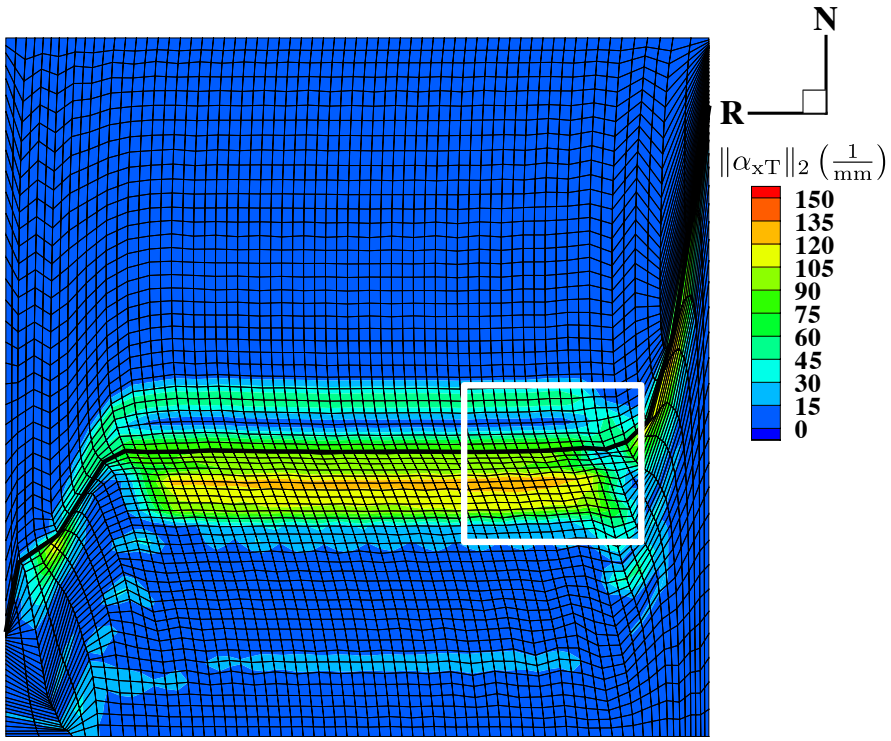

(a) White box indicates approximate area shown in zoomed figure below.

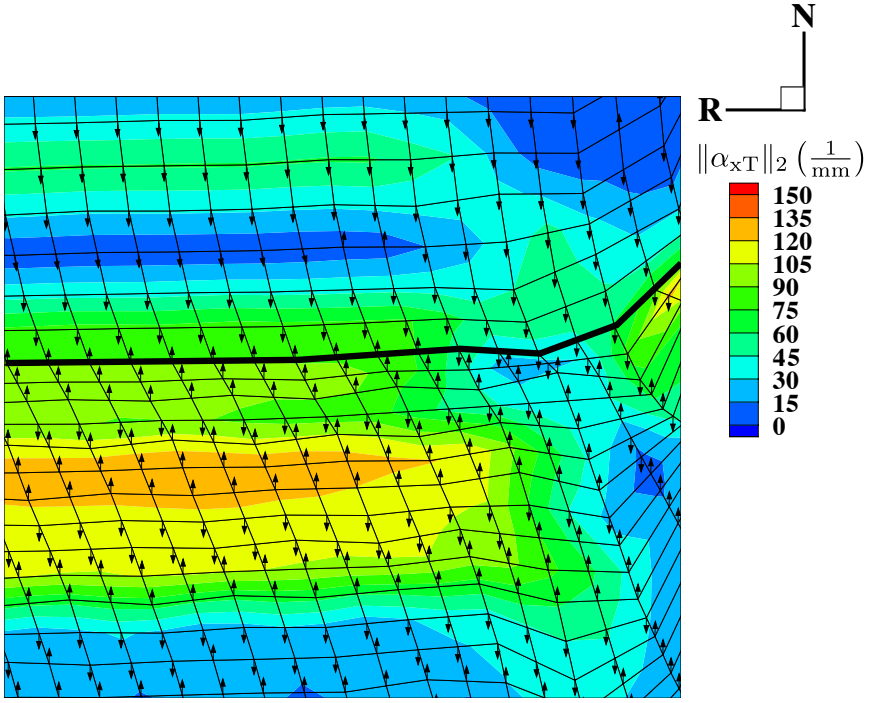

(b) Arrows indicate direction (not magnitude) of vector α_{xT}.

Figure 17: The magnitude of the dislocation density with 'T' line direction, i.e. $\|\alpha_{xT}\|_2 = \sqrt{\alpha_{RT}^2 + \alpha_{TT}^2 + \alpha_{NT}^2}$, at the edge of the grains for the S array at 72% reduction. The images are scaled by a factor of 50 in the N direction. The initial aspect ratio was 4:1:1 (R:T:N).

dislocation distributions within rigid viscoplasticity.

A word about elasticity is important to conclude this paper. In an elastic-plastic setting where the elastic deformation gradient is conceivably composed of an elastic stretch and a rotation, the same conclusions regarding the continuity in the spin and rotation fields may not apply. Let us consider the continuity constraint $[\![\boldsymbol{F}^{e-1}]\!] \times \boldsymbol{n} = \boldsymbol{0}$ when $\boldsymbol{F}^e = \boldsymbol{R}^*\boldsymbol{U}$, where $\boldsymbol{U}$ is an elastic stretch tensor. Our continuity requirement now becomes $[\![\boldsymbol{U}^{-1}\boldsymbol{R}^{*T}]\!] \times \boldsymbol{n} = \boldsymbol{0}$. Certainly for finite elastic stretches (e.g. due to large hydrostatic stress near triple junctions) this requirement is not the same as in the viscoplastic case. Even for small elastic strains it is probable that the addition of elastic interaction may significantly influence results when the continuity indicated in this paper is included in a model.

Classical plasticity modeling is predicated upon independent ODEs for the evolution of state variables. This approach emanates from how the deformation has been described, e.g., the multiplicative decomposition of the deformation gradient. From the results and arguments made herein, it appears that even the problem of size-independent macroscopic plasticity is spatially nonlocal in nature and should be solved accordingly.

Acknowledgments

JCM and AJB gratefully acknowledge financial support through a gift from Caterpillar and funding from NASA, grant no. NNM04AA37G. We also thank Dr. Grethe Winther for discussions and for providing experimental data. A special thanks to the DPLAB at Cornell for providing ODF analysis codes and assistance, especially Donald Boyce. AA gratefully acknowledges the National Science Foundation through the CMU MRSEC, grant no. DMR-0520425

A. Pillbox argument for $\alpha = -\mathrm{curl}\left(\boldsymbol{F}^{e-1}\right) \Rightarrow [\![\boldsymbol{F}^{e-1}]\!] \times \boldsymbol{n} = \boldsymbol{0}$

Following Acharya (2007), we consider a pill box of fixed material particles with a surface of discontinuity s whose normal is $\boldsymbol{n}$, as shown in Fig. 18. Contrary to Acharya (2007), s is not moving with respect to the material.

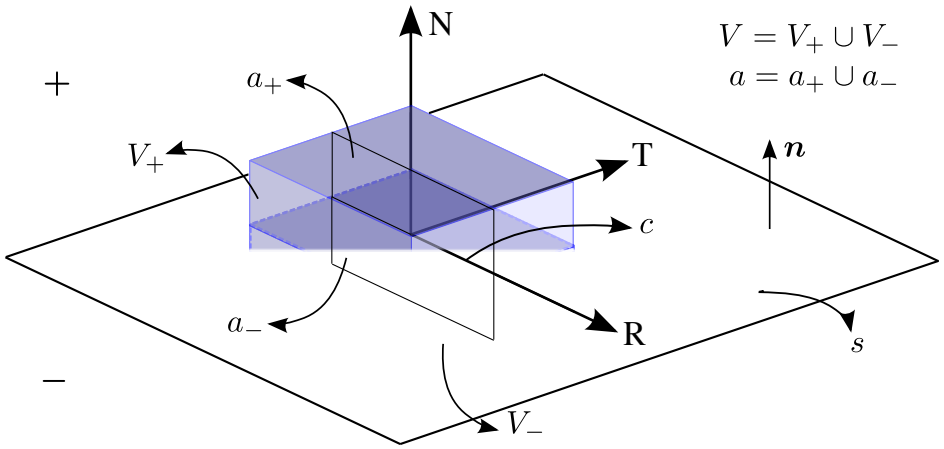

Figure 18: Fixed surface of discontinuity in a deforming material pill box at a fixed instant of time.

The union of the material volumes V_+ and V_- is the material volume V. The arbitrarily oriented material area patch a is the union of the material area patches a_+ and a_-, and the intersection of a and V is the curve c. We denote the unit normal to the area patch a as $\boldsymbol{n}_a$. The limit of fields approaching the surface s from the top is given a subscript '+', and those from the bottom a subscript '-'. If we now integrate the fundamental equation of incompatibility over the area patch a, we have

$$\int_a \boldsymbol{\alpha}\, \boldsymbol{n}_a \, da = -\int_a \operatorname{curl}\left(\boldsymbol{F}^{e-1}\right) \boldsymbol{n}_a \, da = -\int_{\partial a} \boldsymbol{F}^{e-1} \, d\boldsymbol{x} \tag{45}$$

where ∂a is the boundary of a. Let us consider two cases, one where the defect density, $\boldsymbol{\alpha}$, is singular on the surface s and one where $\boldsymbol{\alpha}$ is spread out in the direction perpendicular to s. In the limit of the pill box collapsing onto s and shrinking the curve c to a point, in the former case we are left with

$$\boldsymbol{\alpha}\, \boldsymbol{e}_T = \left[\!\left[\, \boldsymbol{F}^{e-1} \, \right]\!\right] \boldsymbol{e}_R \tag{46}$$

and in the latter case

$$\boldsymbol{0} = \left[\!\left[\, \boldsymbol{F}^{e-1} \, \right]\!\right] \boldsymbol{e}_R \, , \tag{47}$$

where the jump is defined as $\left[\!\left[\, \boldsymbol{F}^{e-1} \, \right]\!\right] = \boldsymbol{F}_+^{e-1} - \boldsymbol{F}_-^{e-1}$. We adopt the latter case and since the tangent direction $\boldsymbol{e}_R$ is arbitrarily oriented on the surface s, another way of writing the continuity condition is

$$\boldsymbol{0} = \left[\!\left[\, \boldsymbol{F}^{e-1} \, \right]\!\right] \times \boldsymbol{e}_N \, , \tag{48}$$

which implies tangential continuity of $\boldsymbol{F}^{e-1}$.

B. Derivation of the incompatibility equation from the conservation law for Burgers vector content

The aim of the following argument is to show that the convected rate equation for the two-point dislocation density tensor (Eq. 10) and the fundamental equation of incompatibility (Eq. 12) imply one another when $\boldsymbol{V} = \boldsymbol{0}$, $\tilde{\boldsymbol{L}}^p = \dot{\boldsymbol{F}}^p \boldsymbol{F}^{p-1} \boldsymbol{F}^{e-1}$, and $\boldsymbol{F} = \boldsymbol{F}^e \boldsymbol{F}^p$. Our calculations are similar to those in Acharya (2004). The convected rate equation is

$$\mathring{\boldsymbol{\alpha}} = -\operatorname{curl}\left(\tilde{\boldsymbol{L}}^p \right) = -\operatorname{curl}\left(\dot{\boldsymbol{F}}^p \boldsymbol{F}^{p-1} \boldsymbol{F}^{e-1} \right) \, . \tag{49}$$

We begin by fixing an arbitrary instant of time, t^*, and write the convected rate equation as

$$\mathring{\boldsymbol{\alpha}}\,(t^*) = -\operatorname{curl}_{t^*}\left(\dot{\boldsymbol{F}}^p\,(t^*)\ \boldsymbol{F}^{p-1}\,(t^*)\ \boldsymbol{F}^{e-1}\,(t^*) \right) \tag{50}$$

where we have suppressed the spatial argument and ( ) means the tensor is a function of the argument in parentheses. Tensors with no such argument are assumed to be functions of the time parameter, t. Using the definition of the

multiplicative decomposition of the deformation gradient we can write

$$\mathring{\boldsymbol{\alpha}}\left(t^*\right) = -\mathrm{curl}_{t^*}\left(\dot{\boldsymbol{F}}^p\left(t^*\right)\ \boldsymbol{F}^{-1}\left(t^*\right)\right) \tag{51}$$

and rewriting the time derivative we have

$$\mathring{\boldsymbol{\alpha}}\left(t^*\right) = -\mathrm{curl}_{t^*}\left(\left[\frac{d}{dt}\ \boldsymbol{F}^p\right]_{t=t^*}\ \boldsymbol{F}^{-1}\left(t^*\right)\right). \tag{52}$$

We can bring $\boldsymbol{F}^{-1}\left(t^*\right)$ inside the time derivative (since it is not a function of time t),

$$\mathring{\boldsymbol{\alpha}}\left(t^*\right) = -\mathrm{curl}_{t^*}\left(\left[\frac{d}{dt}\left(\boldsymbol{F}^p\ \boldsymbol{F}^{-1}\left(t^*\right)\right)\right]_{t=t^*}\right). \tag{53}$$

For the next step we must define the deformation gradient with respect to the configuration at time t^* as,

$$\boldsymbol{F}_{t^*} = \frac{\partial \boldsymbol{x}}{\partial \boldsymbol{x}_{t^*}} \tag{54}$$

where $\boldsymbol{x}$ is the spatial description of the current configuration and $\boldsymbol{x}_{t^*} = \boldsymbol{x}\left(t^*\right)$ is the spatial description of the configuration at time $t = t^*$. Using this definition we can write the total deformation gradient as

$$\boldsymbol{F} = \frac{\partial \boldsymbol{x}}{\partial \boldsymbol{x}_0} = \frac{\partial \boldsymbol{x}}{\partial \boldsymbol{x}_{t^*}}\ \frac{\partial \boldsymbol{x}_{t^*}}{\partial \boldsymbol{x}_0} = \frac{\partial \boldsymbol{x}}{\partial \boldsymbol{x}_{t^*}}\ \frac{\partial \boldsymbol{x}\left(t^*\right)}{\partial \boldsymbol{x}_0} = \boldsymbol{F}_{t^*}\ \boldsymbol{F}\left(t^*\right) \tag{55}$$

where $\boldsymbol{x}_0$ is the spatial description of the reference configuration. Inserting the identity matrix, $\boldsymbol{I} = \boldsymbol{F}_{t^*}^{-1}\ \boldsymbol{F}_{t^*}$, into the argument of the time derivative in Eq. 53 and using the definition of the total deformation gradient in Eq. 55 results in

$$\mathring{\boldsymbol{\alpha}}\left(t^*\right) = -\mathrm{curl}_{t^*}\left(\left[\frac{d}{dt}\left(\boldsymbol{F}^p\ \boldsymbol{F}^{-1}\left(t^*\right)\ \boldsymbol{F}_{t^*}^{-1}\ \boldsymbol{F}_{t^*}\right)\right]_{t=t^*}\right) = -\mathrm{curl}_{t^*}\left(\left[\frac{d}{dt}\left(\boldsymbol{F}^p\ \boldsymbol{F}^{-1}\ \boldsymbol{F}_{t^*}\right)\right]_{t=t^*}\right) \tag{56}$$

The next step is to integrate Eq. 56 over an arbitrary area in the configuration at time t^*,

$$\int_{a_{t^*}} \mathring{\boldsymbol{\alpha}}\left(t^*\right)\ \boldsymbol{n}_{t^*}\ da_{t^*} = \int_{a_{t^*}} -\mathrm{curl}_{t^*}\left(\left[\frac{d}{dt}\left(\boldsymbol{F}^p\ \boldsymbol{F}^{-1}\ \boldsymbol{F}_{t^*}\right)\right]_{t=t^*}\right)\boldsymbol{n}_{t^*}\ da_{t^*} \tag{57}$$

where $\boldsymbol{n}_{t^*}$ is the normal vector to the area a_{t^*}. We must transform both sides of Eq. 57 to obtain the fundamental equation of incompatibility. Continuing with the right hand side (RHS) of Eq. 57 we use the Kelvin-Stokes theorem to transform the surface integral to a line integral, which then allows one to move the time derivative outside of the integral.

$$\int_{a_{t^*}} \mathring{\boldsymbol{\alpha}}\left(t^*\right)\ \boldsymbol{n}_{t^*}\ da_{t^*} = -\left\{\frac{d}{dt}\int_{\partial a_{t^*}} \boldsymbol{F}^p\ \boldsymbol{F}^{-1}\ \boldsymbol{F}_{t^*}\ d\boldsymbol{x}_{t^*}\right\}_{t=t^*} \tag{58}$$

The RHS is then transformed to the current configuration using the definition of the deformation gradient $\boldsymbol{F}_{t^*}$, and written in terms of the inverse elastic distortion using the definition of the total deformation gradient $\boldsymbol{F}$,

$$\int_{a_{t^*}} \mathring{\boldsymbol{\alpha}}\,(t^*)\ \boldsymbol{n}_{t^*}\ da_{t^*} = -\left\{\frac{d}{dt}\int_{\partial a_t} \boldsymbol{F}^p\ \boldsymbol{F}^{-1}\ d\boldsymbol{x}_t\right\}_{t=t^*} = -\left\{\frac{d}{dt}\int_{\partial a_t} \boldsymbol{F}^{e-1}\ d\boldsymbol{x}_t\right\}_{t=t^*} \tag{59}$$

and then transformed back to a surface integral using the Kelvin-Stokes theorem again.

$$\int_{a_{t^*}} \mathring{\boldsymbol{\alpha}}\,(t^*)\ \boldsymbol{n}_{t^*}\ da_{t^*} = -\left\{\frac{d}{dt}\int_{a_t} \operatorname{curl}\Big(\ \boldsymbol{F}^{e-1}\ \Big)\ \boldsymbol{n}_t\ da_t\right\}_{t=t^*} \tag{60}$$

Thus far we have obtained an equation containing part of the fundamental equation of incompatibility, i.e., $\operatorname{curl}\Big(\ \boldsymbol{F}^{e-1}\ \Big)$. We now proceed with transforming the left hand side (LHS) of Eq. 60, which may be rewritten as,

$$\int_{a_{t^*}} \frac{d}{dt}\Big[\ J_{t^*}\ \boldsymbol{\alpha}\ \boldsymbol{F}_{t^*}^{-T}\ \Big]_{t=t^*}\ \boldsymbol{n}_{t^*}\ da_{t^*} = -\left\{\frac{d}{dt}\int_{a_t} \operatorname{curl}\Big(\ \boldsymbol{F}^{e-1}\ \Big)\ \boldsymbol{n}_t\ da_t\right\}_{t=t^*} \tag{61}$$

where $J_{t^*} = \det(\boldsymbol{F}_{t^*})$. We now show the equivalence between the arguments in the LHS integrals of Eqs. 60 and 61, and begin by expanding the time derivative of the integral argument in Eq. 61.

$$\left[\frac{d}{dt}\ \Big(J_{t^*}\ \boldsymbol{\alpha}\ \boldsymbol{F}_{t^*}^{-T}\ \Big)\right]_{t=t^*} = \Big[\ \dot{J}_{t^*}\ \boldsymbol{\alpha}\ \boldsymbol{F}_{t^*}^{-T} + J_{t^*}\ \dot{\boldsymbol{\alpha}}\ \boldsymbol{F}_{t^*}^{-T} + J_{t^*}\ \boldsymbol{\alpha}\ \dot{\boldsymbol{F}}_{t^*}^{-T}\ \Big]_{t=t^*} \tag{62}$$

Before proceeding further we need to write the velocity gradient $\boldsymbol{L}$ in terms of the deformation gradient based on the arbitrary configuration at time t^*. Using the definition of $\boldsymbol{F}$ from Eq. 55 we can write

$$\boldsymbol{L} = \dot{\boldsymbol{F}}\ \boldsymbol{F}^{-1} = \dot{\boldsymbol{F}}_{t^*}\ \boldsymbol{F}\,(t^*)\ \ \boldsymbol{F}^{-1}\,(t^*)\ \ \boldsymbol{F}_{t^*}^{-1} = \dot{\boldsymbol{F}}_{t^*}\ \boldsymbol{F}_{t^*}^{-1}\ . \tag{63}$$

The time derivative of the Jacobian determinant in the first term in Eq. 62 is expanded as

$$\dot{J}_{t^*} = \frac{d}{dt}\left(\ \det(\boldsymbol{F}_{t^*})\ \right) = \det(\boldsymbol{F}_{t^*})\ \ \operatorname{tr}\Big(\boldsymbol{F}_{t^*}^{-1}\ \dot{\boldsymbol{F}}_{t^*}\Big) = J_{t^*}\ \operatorname{tr}(\boldsymbol{L}) = J_{t^*}\ \ (\operatorname{div}\boldsymbol{v}) \tag{64}$$

where $\boldsymbol{v}$ is the velocity field. The time derivative in the third term in Eq. 62 is expanded as

$$\dot{\boldsymbol{F}}_{t^*}^{-T} = -\boldsymbol{F}_{t^*}^{-T}\ \dot{\boldsymbol{F}}_{t^*}^{T}\ \boldsymbol{F}_{t^*}^{-T} = \boldsymbol{L}^T\ \boldsymbol{F}_{t^*}^{-T}\ . \tag{65}$$

Using the results of Eqs. 64 and 65 we can rewrite Eq. 62 in terms of the convected derivative (cf. Eq. 10) and evaluate at time $t = t^*$.

$$\left[\frac{d}{dt}\ \Big(\ J_{t^*}\ \boldsymbol{\alpha}\ \boldsymbol{F}_{t^*}^{-T}\ \Big)\right]_{t=t^*} = \Big\{\ J_{t^*}\ \Big[\ (\operatorname{div}\boldsymbol{v})\ \ \boldsymbol{\alpha} + \dot{\boldsymbol{\alpha}} + \boldsymbol{\alpha}\ \boldsymbol{L}^T\ \Big]\ \boldsymbol{F}_{t^*}^{-T}\ \Big\}_{t=t^*} = \Big\{\ J_{t^*}\ \mathring{\boldsymbol{\alpha}}\ \boldsymbol{F}_{t^*}^{-T}\ \Big\}_{t=t^*} = \mathring{\boldsymbol{\alpha}}\,(t^*)\ . \tag{66}$$

Now that we have shown that $\mathring{\boldsymbol{\alpha}}\,(t^*)$ and $\left[\frac{d}{dt}\left(\, J_{t^*}\;\boldsymbol{\alpha}\;\boldsymbol{F}_{t^*}^{-T}\,\right)\right]_{t=t^*}$ are equivalent we continue the derivation from Eq. 61. The time derivative is moved outside of the LHS integral and using Nanson's formula we can transform the LHS integral to the current configuration.

$$\left\{\frac{d}{dt}\int_{a_t}\boldsymbol{\alpha}\;\boldsymbol{n}_t\;da_t\right\}_{t=t^*} = -\left\{\frac{d}{dt}\int_{a_t}\operatorname{curl}\left(\,\boldsymbol{F}^{e-1}\,\right)\;\boldsymbol{n}_t\;da_t\right\}_{t=t^*} \tag{67}$$

Equation 67 implies the fundamental equation of incompatibility, $\operatorname{curl}\left(\boldsymbol{F}^{e-1}\right) = -\boldsymbol{\alpha}$, for all time t, given that it holds at time $t = 0$ and because t^* was chosen arbitrarily.

C. Derivation of a continuous rotation field from the continuity condition on $\boldsymbol{R}^{*T}$

The following will show that the continuity condition $[\![\,\boldsymbol{R}^{*T}\,]\!]\times\boldsymbol{n} = \boldsymbol{0}$ implies a continuous rotation field. First we expand the jump argument as

$$[\![\,\boldsymbol{R}^{*T}\,]\!]\times\boldsymbol{n} = \boldsymbol{0} \;\Rightarrow\; \left(\boldsymbol{R}_+^{*T} - \boldsymbol{R}_-^{*T}\right)\times\boldsymbol{n} = \boldsymbol{0}\,. \tag{68}$$

We assume that $\boldsymbol{R}_+^{*T}$ and $\boldsymbol{R}_-^{*T}$ are proper orthogonal tensors, i.e. for a proper orthogonal tensor $\boldsymbol{A}$, $\boldsymbol{A}^T = \boldsymbol{A}^{-1}$ and $\det\boldsymbol{A} = +1$. Since $\boldsymbol{R}_+^{*T}$ and $\boldsymbol{R}_-^{*T}$ are invertible we choose to multiply the continuity condition from the left by $-\boldsymbol{R}_+^{*}$ which leaves us with

$$(\,\boldsymbol{Q}-\boldsymbol{I}\,)\times\boldsymbol{n} = \boldsymbol{0}\,, \tag{69}$$

where $\boldsymbol{Q} = \boldsymbol{R}_+^{*}\,\boldsymbol{R}_-^{*T}$ and $\boldsymbol{I}$ is the identity tensor. Without loss of generality we choose an orthonormal basis whose $\boldsymbol{e}_3$ is the direction $\boldsymbol{n}$ of the interface. Solving this equation for $(\,\boldsymbol{Q}-\boldsymbol{I}\,)$ tells us that

$$(\,\boldsymbol{Q}-\boldsymbol{I}\,) = \boldsymbol{a}\otimes\boldsymbol{n} \tag{70}$$

where $\boldsymbol{a} = \left\langle\,\frac{z_1}{n_3},\frac{z_2}{n_3},\frac{z_3-1}{n_3}\,\right\rangle$ and $(\,z_1,z_2,z_3\,)$ are arbitrary real numbers. We then require that $\boldsymbol{Q}$ be a proper orthogonal tensor because it is the product of two proper orthogonal tensors. Enforcing the conditions $\boldsymbol{Q}^T = \boldsymbol{Q}^{-1}$ and $\det\boldsymbol{Q} = +1$ yields the solution $z_1 = z_2 = 0,\; z_3 = 1$, resulting in

$$(\,\boldsymbol{Q}-\boldsymbol{I}\,) = \boldsymbol{0} \;\Rightarrow\; \boldsymbol{Q} = \boldsymbol{I}\,. \tag{71}$$

Since $\boldsymbol{Q}$ must equal the identity tensor we can conclude that

$$\boldsymbol{Q} = \boldsymbol{I} \;\Rightarrow\; \boldsymbol{R}_+^{*} = \boldsymbol{R}_-^{*} \;\Rightarrow\; [\![\,\boldsymbol{R}^{*}\,]\!] = [\![\,\boldsymbol{R}^{*T}\,]\!] = \boldsymbol{0}\,. \tag{72}$$

Another way to think of this geometrically is that the two rotations must agree on their action on a plane of vectors (cf. Eq. 47). Now, what can happen to the action of $\boldsymbol{Q}$ on the normal? The magnitude must be preserved; the direction must also be preserved, otherwise it would change the included angle between the undeformed normal and a vector in the invariant plane. Therefore, $\boldsymbol{Q}$ is the identity tensor. We begin with the following.

$$\begin{aligned} &\left(\boldsymbol{R}_{+}^{*T} - \boldsymbol{R}_{-}^{*T}\right)\boldsymbol{e}_t = \boldsymbol{0} \quad \forall\, \boldsymbol{e}_t \quad \text{s.t.} \;\; \boldsymbol{e}_t \cdot \boldsymbol{n} = 0 \\ &\Rightarrow \boldsymbol{Q}\boldsymbol{e}_t = \boldsymbol{e}_t\,, \quad \boldsymbol{Q} := \boldsymbol{R}_{+}^{*}\,\boldsymbol{R}_{-}^{*T} \end{aligned} \tag{73}$$

The action of an orthogonal tensor preserves magnitudes of vectors and angles between vectors, and so we have

$$\boldsymbol{Q}\boldsymbol{n} \cdot \boldsymbol{Q}\boldsymbol{e}_t = \boldsymbol{n} \cdot \boldsymbol{e}_t = 0\,, \tag{74}$$

however, $\boldsymbol{Q}\boldsymbol{e}_t = \boldsymbol{e}_t \quad \forall\, \boldsymbol{e}_t \quad \text{s.t.} \;\; \boldsymbol{e}_t \cdot \boldsymbol{n} = 0$, therefore,

$$\begin{aligned} &\boldsymbol{Q}\boldsymbol{n} \cdot \boldsymbol{e}_t = 0 \\ &\Rightarrow \boldsymbol{Q}\boldsymbol{n} \;\parallel\; \boldsymbol{n}\,. \end{aligned} \tag{75}$$

Also, $|\boldsymbol{Q}\boldsymbol{n}| = |\boldsymbol{n}|$, since $\boldsymbol{Q}$ is orthogonal. Now let $(\boldsymbol{e}_{t1}, \boldsymbol{e}_{t2}, \boldsymbol{n})$ be an orthonormal basis where the first two vectors of the basis belong to the invariant plane. Since $\boldsymbol{Q}$ is **proper** orthogonal, by definition

$$\begin{aligned} &\det \boldsymbol{Q} = \frac{\boldsymbol{Q}\boldsymbol{n} \cdot (\boldsymbol{Q}\boldsymbol{e}_{t1} \times \boldsymbol{Q}\boldsymbol{e}_{t2})}{\boldsymbol{n} \cdot (\boldsymbol{e}_{t1} \times \boldsymbol{e}_{t2})} = \boldsymbol{Q}\boldsymbol{n} \cdot (\boldsymbol{e}_{t1} \times \boldsymbol{e}_{t2}) = +1 \\ &\Rightarrow \boldsymbol{Q}\boldsymbol{n} \cdot \boldsymbol{n} = +1\,. \end{aligned} \tag{76}$$

Together, $\boldsymbol{Q}\boldsymbol{n} \;\parallel\; \boldsymbol{n}$, $|\boldsymbol{Q}\boldsymbol{n}| = |\boldsymbol{n}|$, and $\boldsymbol{Q}\boldsymbol{n} \cdot \boldsymbol{n} = +1$, imply $\boldsymbol{Q}\boldsymbol{n} = \boldsymbol{n}$. Since $\boldsymbol{Q}$ agrees with the identity tensor on an orthonormal basis (actually we have shown more), they are identical tensors.

References

J. Hirsch, K. Lücke, Mechanism of Deformation and Development of Rolling Textures in Polycrystalline F.C.C. Metals—II. Simulation and Interpretation of Experiments on the Basis of Taylor-Type Theories, Acta Metallurgica 36 (11) (1988) 2883–2904.

R. E. Bolmaro, A. Fourty, A. Roatta, M. A. Bertinetti, P. A. Turner, J. W. Signorelli, A New Approach to Crystal Spin Calculation During Deformation Texture Development, Scripta Materialia 43 (2000) 553–559.

C. N. Tomé, R. A. Lebensohn, C. T. Necker, Mechanical Anisotropy and Grain Interaction in Recrystallized Aluminum, Metallurgical and Materials Transactions A 33A (2002) 2635–2648.

R. E. Bolmaro, A. Fourty, J. W. Signorelli, H.-G. Brokmeier, Development of wire drawing textures in Cu-Fe: the influence of macroscopic and microscopic heterogeneities, Modelling and Simulation in Materials Science and Engineering 14 (2006) 1–19.

J. W. Signorelli, P. A. Turner, V. Sordi, M. Ferrante, E. A. Vieira, R. E. Bolmaro, Computational modeling of texture and microstructure evolution in Al alloys deformed by ECAE, Scripta Materialia 55 (2006) 1099–1102.

R. E. Bolmaro, A. Roatta, A. L. Fourty, J. W. Signorelli, Recrystallization textures in fcc materials: A simulation based on micromechanical modeling data, Scripta Materialia 53 (2005) 147–152.

A. Acharya, A. Roy, Size effects and idealized dislocation microstructure at small scales: Predictions of Phenomenological model of Mesoscopic Field Dislocation Mechanics: Part I, Journal of the Mechanics and Physics of Solids 54 (2006) 1687–1710.

A. Roy, A. Acharya, Size effects and idealized dislocation microstructure at small scales: Predictions of Phenomenological model of Mesoscopic Field Dislocation Mechanics: Part II, Journal of the Mechanics and Physics of Solids 54 (2006) 1711–1743.

S. Varadhan, Modeling Collective Behavior of Dislocations in Crystalline Materials, Ph.D. thesis, University of Illinois at Urbana-Champaign, 2007.

M. E. Gurtin, A. Needleman, Boundary conditions in small-deformation single-crystal plasticity that account for the Burgers vector, Journal of the Mechanics and Physics of Solids 53 (2005) 1–31.

K. K. Mathur, P. R. Dawson, On Modeling the Development of Crystallographic Texture in Bulk Forming Processes, International Journal of Plasticity 5 (1989) 67–94.

A. Acharya, Jump condition for GND evolution as a constraint on slip transmission at grain boundaries, Philosophical Magazine 87 (8–9) (2007) 1349–1359.

R. T. Shield, The Rotation Associated with Large Strains, SIAM Journal of Applied Mathematics 25 (3) (1973) 483–491.

T. Mura, Continuous distribution of moving dislocations, Philosophical Magazine 89 (1963) 843–857.

A. Acharya, Constitutive analysis of finite deformation field dislocation mechanics, Journal of the Mechanics and Physics of Solids 52 (2004) 301–316.

J. F. Nye, Some geometrical relations in dislocated crystals, Acta Metallurgica 1 (1953) 153–162.

A. Acharya, A model of crystal plasticity based on the theory of continuously distributed dislocations, Journal of the Mechanics and Physics of Solids 49 (761–784).

A. Acharya, A. Beaudoin, R. Miller, New perspectives in Plasticity Theory: Dislocation Nucleation, Waves, and Partial Continuity of the Plastic Strain Rate, Mathematics and Mechanics of Solids 13 (2008) 292–315.

J. R. Willis, Second-order Effects of Dislocations in Anisotropic Crystals, International Journal of Engineering Science 5 (1967) 171–190.

N. Fox, A Continuum Theory of Dislocations for Single Crystals, IMA Journal of Applied Mathematics 2 (4) (1966) 285–298.

A. Acharya, J. L. Bassani, Lattice incompatibility and a gradient theory of crystal plasticity, Journal of the Mechanics and Physics of Solids 48 (2000) 1565–1595.

E. Kröner, Allgemeine Kontinuumstheorie der Versetzungen und Eigenspannungen, Archive for Rational Mechanics and Analysis 4 (1) (1959) 273–334.

E. H. Lee, D. T. Liu, Finite-Strain Elastic-Plastic Theory with Application to Plane-Wave Analysis, Journal of Applied Physics 38 (1) (1967) 19–27.

E. H. Lee, Elastic-Plastic Deformation at Finite Strains, Journal of Applied Mechanics 36 (1969) 1–6.

J. Kratochvil, On a Finite Strain Theory of Elastic-Inelastic Materials, Acta Mechanica 16 (1973) 127–142.

E. H. Lee, Finite Deformation Theory with Nonlinear Kinematics, in: E. H. Lee, R. L. Mallet (Eds.), Plasticity of Metals at Finite Strain, Division of Applied Mechanics, Stanford University, Department of Mechanical Engineering, RPI, 107–120, 1982.

H. Honneff, H. Mecking, A Method for the Determination of the Active Slip Systems and Orientation Changes During Single Crystal Deformation, in: G. Gottstein, K. Lücke (Eds.), Textures of Materials, Proceedings of ICOTOM V, Springer, Berlin, 265–275, 1978.

P. Van Houtte, L. Delannay, I. Samajdar, Quantitative Prediction of Cold Rolling Textures in Low-Carbon Steel by Means of the LAMEL Model, Textures and Microstructures 31 (1999) 109–149.

P. Van Houtte, S. Li, M. Seefeldt, L. Delannay, Deformation Texture Prediction: from the Taylor Model to the Advanced LAMEL model, International Journal of Plasticity 21 (2005) 589–624.

B. J. Lee, S. Ahzi, D. M. Parks, Bicrystal-Based Modeling of Plasticity in FCC Metals, Journal of Engineering Materials and Technology 124 (2002) 27–40.

R. E. Bolmaro, R. A. Lebensohn, H.-G. Brokmeier, Crystal spin in two-sites self consistent models: From kinematics to kinetics, Computational

Materials Science 9 (1997) 237–250.

A. J. Beaudoin, P. R. Dawson, K. K. Mathur, U. F. Kocks, D. A. Korzekwa, Application of polycrystal plasticity to sheet forming, Computer Methods in Applied Mechanics and Engineering 117 (1994) 49–70.

O. C. Zienkiewicz, J. P. Vilotte, S. Toyoshima, S. Nakazawa, Iterative Method for Constrained and Mixed Appproximation. An Inexpensive Improvement for F.E.M. performanace, Computer Methods in Applied Mechanics and Engineering 51 (1985) 3–29.

A. J. Beaudoin, P. R. Dawson, K. K. Mathur, U. F. Kocks, A hybrid finite element formulation for polycrystal plasticity with consideration of macrostructural and microstructural linking, International Journal of Plasticity 11 (5) (1995) 501–521.

G. M. Eggert, P. R. Dawson, K. K. Mathur, An Adaptive Descent Method for Non-Linear Viscoplasticity, International Journal of Numerical Methods in Engineering 31 (1991) 1031–1054.

The Mathworks, Inc., MATLAB®, 2008.

P. Dawson, D. Boyce, et al., The DPLAB Polycrystal Library at Cornell, 2008.

A. Kumar, P. R. Dawson, Computational Modeling of F.C.C. Deformation Textures over Rodrigues' Space, Acta Materialia 48 (2000) 2719–2736.

G. Winther, L. Margulies, S. Schmidt, H. F. Poulsen, Lattice rotations of individual bulk grains Part II: correlation with initial orientation and model comparison, Acta Materialia 52 (2004) 2863–2872.

J. A. Wert, C. T. Thorning, Grain subdivision in polycrystalline copper subject to tensile deformation, Materials Science and Technology 21 (12) (2005) 1401–1406.

A. J. Beaudoin, H. Mecking, U. F. Kocks, Development of localized orientation gradients in fcc polycrystals, Philosophical Magazine 74 (6) (1996) 1503–1517.

A. J. Beaudoin, A. Acharya, S. R. Chen, D. A. Korzekwa, M. G. Stout, Consideration of grain-size effect and kinetics in the plastic deformation of metal polycrystals, Acta Materialia 48 (2000) 3409–3423.

A. Acharya, A. J. Beaudoin, Grain-size effect in viscoplastic polycrystals at moderate strains, Journal of the Mechanics and Physics of Solids 48 (2000) 2213–2230.

A. J. Beaudoin, A. Acharya, A model for rate-dependent flow of metal polycrystals based on the slip plane lattice incompatibility, Materials Science and Engineering A 309–310 (2001) 411–415.

S. Kok, A. J. Beaudoin, D. A. Tortorelli, On the development of stage IV hardening using a model based on the mechanical threshold, Acta Materialia 50 (2002) 1653–1667.

J. W. Kysar, Y. X. Gan, T. L. Morse, X. Chen, M. E. Jones, High strain gradient plasticity associated with wedge indentation into face-centered cubic single crystals: Geometrically necessary dislocation densities, Journal of the Mechanics and Physics of Solids 55 (2007) 1554–1573.